Multifaceted control of E-cadherin dynamics by Adaptor Protein Complex 1 during epithelial morphogenesis

Miguel Ramírez Moreno, Katy Boswell, Helen L. Casbolt, and Natalia A. Bulgakova*
School of Biosciences and Bateson Centre, The University of Sheffield, Sheffield S10 2TN, UK

ABSTRACT **Intracellular trafficking regulates the distribution of transmembrane proteins including the key determinants of epithelial polarity and adhesion. The Adaptor Protein 1 (AP-1) complex is the key regulator of vesicle sorting, which binds many specific cargoes. We examined roles of the AP-1 complex in epithelial morphogenesis, using the *Drosophila* wing as a paradigm. We found that AP-1 knockdown leads to ectopic tissue folding, which is consistent with the observed defects in integrin targeting to the basal cell–extracellular matrix adhesion sites. This occurs concurrently with an integrin-independent induction of cell death, which counteracts elevated proliferation and prevents hyperplasia. We discovered a distinct pool of AP-1 that localizes at the subapical adherens junctions. Upon AP-1 knockdown, E-cadherin is hyperinternalized from these junctions and becomes enriched at the Golgi and recycling endosomes. We then provide evidence that E-cadherin hyperinternalization acts upstream of cell death in a potential tumor-suppressive mechanism. Simultaneously, cells compensate for elevated internalization of E-cadherin by increasing its expression to maintain cell–cell adhesion.**

Monitoring Editor
Richard Fehon
University of Chicago

Received: Dec 6, 2021
Revised: Apr 15, 2022
Accepted: May 17, 2022

INTRODUCTION

Epithelial morphogenesis gives origin to complex structures from simple epithelial sheets (Schock and Perrimon, 2002). It is driven by changes in the properties of the cells, often influenced by adhesion molecules (Schock and Perrimon, 2002; Heisenberg and Bellaïche, 2013). These transmembrane molecules constitute the cornerstone of interactions between individual cells and with their environment, enabling morphogenetic processes (Gumbiner, 1996; Halbleib and Nelson, 2006). E-cadherin (E-cad, encoded by the *shotgun* gene in *Drosophila*) is one of the cell–cell adhesion molecules that connect neighboring cells at the subapical adherens junctions (AJs) in epithelial cells (Takeichi, 1977; Harris and Peifer, 2004). E-cad contributes to numerous developmental processes and diseases such as cancer (Halbleib and Nelson, 2006; Brüser and Bogdan, 2017; Janiszewska *et al.*, 2020). Basally, integrins anchor cells to the extracellular matrix, controlling tissue folding but also linking the cell architecture and intracellular signaling (Yamada and Miyamoto, 1995; Domínguez-Giménez *et al.*, 2007; Lee and Streuli, 2014; Sui *et al.*, 2018). The regulation of the cell surface presentation of these adhesion proteins and their impact on tissue morphogenesis remain open questions in the fields of cell and developmental biology (Nanes and Kowalczyk, 2012).

Intracellular trafficking represents one of the main ways to regulate protein presentation at the cell surface (Grant and Donaldson, 2009; Herrmann and Spang, 2015). Cargo-containing vesicles are sent from and to numerous organelles, with the trans-Golgi network (TGN) and recycling endosomes (REs) serving as the main sorting centers in the cell (Grant and Donaldson, 2009; Eaton and Martin-Belmonte, 2014; Tan *et al.*, 2019). Most of what is known about trafficking pathways and their key regulators comes from studies in single cells, which yield a great molecular data output but do not inform about their functions in tissue contexts during development (Fölsch *et al.*, 2001; Guo *et al.*, 2012; Brüser and Bogdan, 2017; Huang *et al.*, 2019; York *et al.*, 2020).

This article was published online ahead of print in MBoC in Press (http://www.molbiolcell.org/cgi/doi/10.1091/mbc.E21-12-0598) on May 24, 2022.

Competing interests: The authors declare no competing interests.

*Address correspondence to: Natalia A. Bulgakova (n.bulgakova@sheffield.ac.uk).

Abbreviations used: A, anterior; AJ, adherens junctions; AP-1, adaptor protein complex 1; BM, basal membrane; E-cad, E-cadherin; MCC_{diff}, Manders's colocalization coefficients; P, posterior; REs, recyclilng endosomes; TGN, trans-Golgi network.

One of the key regulators of intracellular trafficking is the Adaptor Protein Complex 1 (AP-1), shuttling vesicles within the TGN/RE continuum (Bonifacino and Rojas, 2006; Bonifacino, 2014; Grant and Donaldson, 2009; Tan *et al.*, 2019). It is a heterotetrameric complex consisting of two large subunits (γ and β), one medium subunit (μ), and one small subunit (σ) (Nakatsu *et al.*, 2014). Two mammalian isoforms exist, depending on the participant μ subunit: the μ1-containing ubiquitously expressed AP-1A and the μ2-containing epithelia-specific AP-1B (Gravotta *et al.*, 2007, 2012; Hase *et al.*, 2013; Fölsch, 2015). Although the mammalian μ subunits are 79% identical, AP-1A sorts basolateral cargoes at the TGN, where it is recruited by the small GTPase Arf1 (Fölsch *et al.*, 2003; Gravotta *et al.*, 2012; Ren *et al.*, 2013; Sauvageau *et al.*, 2017), and AP-1B sorts proteins from REs to the basolateral membrane and is regulated by the small GTPase Arf6 (Shteyn *et al.*, 2011). AP-1B is also found at integrin-mediated focal adhesions, and its loss correlates with the migratory behavior of metastatic cells (Kell *et al.*, 2020). Two AP-1s are also found in *Caenorhabditis elegans*, where they restrict the basolateral localization of E-cad (Shafaq-Zadah *et al.*, 2012; Gillard *et al.*, 2015). In the fruit fly, *Drosophila melanogaster*, a single AP-1 complex localizes to both TGN and REs and is required for the maintenance of E-cad at the ring canals during oogenesis (Benhra *et al.*, 2011; Burgess *et al.*, 2011; Loyer *et al.*, 2015). In epithelia, the fly AP-1 has been linked to the distribution of Notch pathway components only in specialized cells—the retina and sensory organs (Benhra *et al.*, 2011; Kametaka *et al.*, 2012; Loyer *et al.*, 2015). There, it is one of the pathways that modulates the trafficking of Notch toward E-cad junctions (Benhra *et al.*, 2011; Bellec *et al.*, 2021). Curiously, more Notch accumulates at these junctions upon loss of AP-1, which was attributed to elevated apical targeting at the expense of basolateral targeting without apparent defects in cell polarity and E-cad adhesion.

In this work, we demonstrate that the *Drosophila* AP-1 complex is necessary for epithelial morphogenesis using the developing wing as a paradigm. There, the AP-1 complex influences cell size and number, tissue folding and controls the transport of E-cad and integrins. We identified a distinct subapical pool of the AP-1 complex and determined that the AP-1 complex modulates the endocytosis of E-cad. The excessive internalization of E-cad following AP-1 knockdown triggers cell death, which counteracts elevated proliferation and suppresses hyperplasia: overgrowth without disrupting the epithelial architecture (Hariharan and Bilder, 2006). The surface levels of E-cad remain, however, stable due to adjusted expression. Altogether, our results demonstrate the versatility of functions of the AP-1 complex in intracellular trafficking in vivo and link it to tissue development and pathology.

RESULTS

We employed the GAL4/UAS system (Brand and Perrimon, 1993) and the *engrailed* promoter (*en-GAL4*) to knock down AP-1 using RNA interference (RNAi) throughout development in the posterior compartments of the wing primordia (imaginal discs; Figure 1, A–C). Down-regulation of AP-1μ or AP-1γ (Supplemental Figure S1A)—two unique subunits of the AP-1 complex (Robinson, 2004; Tan *et al.*, 2019)—led to defective morphology of adult wings, ranging from absent to severely disrupted posterior compartments (Figure 1A). A similar adult phenotype was caused by using the *MS1096*-GAL4 driver (Supplemental Figure S1B), which expresses GAL4 throughout the wing pouch (presumptive region of the adult wing; Figure 1C).

We observed complex morphological changes upon AP-1μ or AP-1γ knockdown already in third instar wing imaginal discs (Figure 1, B–E). Posterior compartments were reduced in size, as reflected by their posterior:anterior (P:A) compartment ratio (Figure 1, B and D). AP-1 knockdown resulted in ectopic folding of the wing pouch region, although compartmental borders remained well defined in the disc (Figure 1E). While this folding could contribute to the reduced compartment size, we also examined the apical cell area and found that it was increased, as detected with GFP-tagged E-cad expressed from the endogenous locus (the knockin of GFP into *shg* gene, *shg*-E-cad::GFP; Figure 1, F and G; Huang *et al.*, 2009). Combining the apical cell area increase with the reduced size of compartments indicated a decrease in the total number of cells in the monolayer epithelium of the wing pouch. This could be a consequence of a reduced proliferation rate, increase in cell death, or extrusion of live cells. However, the proliferation rate was increased when normalized to cell number, although the rate on the tissue level was unaffected (Supplemental Figure S1, C–E). Concurrently, we detected considerable cell death visualized by the cleaved effector caspase Dcp-1 (Figure 1H and Supplemental Figure S1F), which was accompanied by fragmented DAPI (a fluorescent stain that binds DNA) staining, indicative of nuclear debris (Supplemental Figure S1G). The basal localization of Dcp-1 and fragmented DAPI (Figure 1H and Supplemental Figure S1, F and G) suggests that these are dying cells being eliminated and extruded (Bergantiños *et al.*, 2010; Herrera *et al.*, 2013). Consistent with these changes in cell proliferation and death, coexpression of AP-1μ RNAi with the apoptosis-blocking baculoviral p35 protein, which blocks effector caspases but not their processing (Hay *et al.*, 1994; Fan and Bergmann, 2008; Martín *et al.*, 2009), caused hyperplastic growth (Figure 1I). These cells still exhibited the increased apical cell area (Supplemental Figure S1, H and I), suggesting that it is not a simple consequence of a decreased cell number due to apoptosis. Therefore, the three main effects of AP-1 knockdown in wing imaginal discs are increased cell death, enlarged apical cell area, and ectopic folds.

As ectopic folds can be due to altered basal adhesion (Sui *et al.*, 2018), we examined integrin localization upon AP-1 knockdown. The αPS1 (Mew) integrin—specific for the dorsal compartment (Brower *et al.*, 1984)—was nearly absent from the basal surface of the tissue (Figure 2A). We found similar changes in the distribution of αPS1 binding partner, βPS (Mys), and Laminin B2 (Supplemental Figure S2A), further supporting the loss of basal adhesions. Mimicking this loss by overexpressing diβ, a dominant negative version of Mys that displaces endogenous protein (Figure 2B) (Martin-Bermudo *et al.*, 1999; Domínguez-Giménez *et al.*, 2007), led to ectopic folds similar to that in AP-1 knockdown (Figure 2C) (Domínguez-Giménez *et al.*, 2007). This correlated with the absence of αPS1 at the posterior compartment (Figure 2D), akin to the effects of AP-1 knockdown (Figure 2A). However, diβ expression did not increase the apical cell area (Figure 2, E and F) and caused only small pockets of dying cells (Figure 2G) in contrast to AP-1 knockdown. These results are consistent with AP-1 down-regulation leading to ectopic folding due to disruption of the basal localization of integrins. However, the effects of AP-1 down-regulation on cell survival appear to be through an integrin-independent mechanism.

To gain insights into this mechanism, we explored the intracellular localization of the AP-1 complex using the Venus-tagged AP-1μ (AP-1μ::VFP) (Benhra *et al.*, 2011). Consistent with other cell types (Grant and Donaldson, 2009; Benhra *et al.*, 2011; Burgess *et al.*, 2011; Tan *et al.*, 2019), AP-1μ::VFP accumulated within puncta (spots) matching the TGN (Golgin-245–positive [Kondylis and Rabouille, 2009; Riedel *et al.*, 2016]; Figure 3A) and REs (Rab11-positive; Figure 3A [Tanaka *et al.*, 2008]). Unexpectedly, we also found a distinct subapical pool of AP-1μ colocalizing with E-cad at

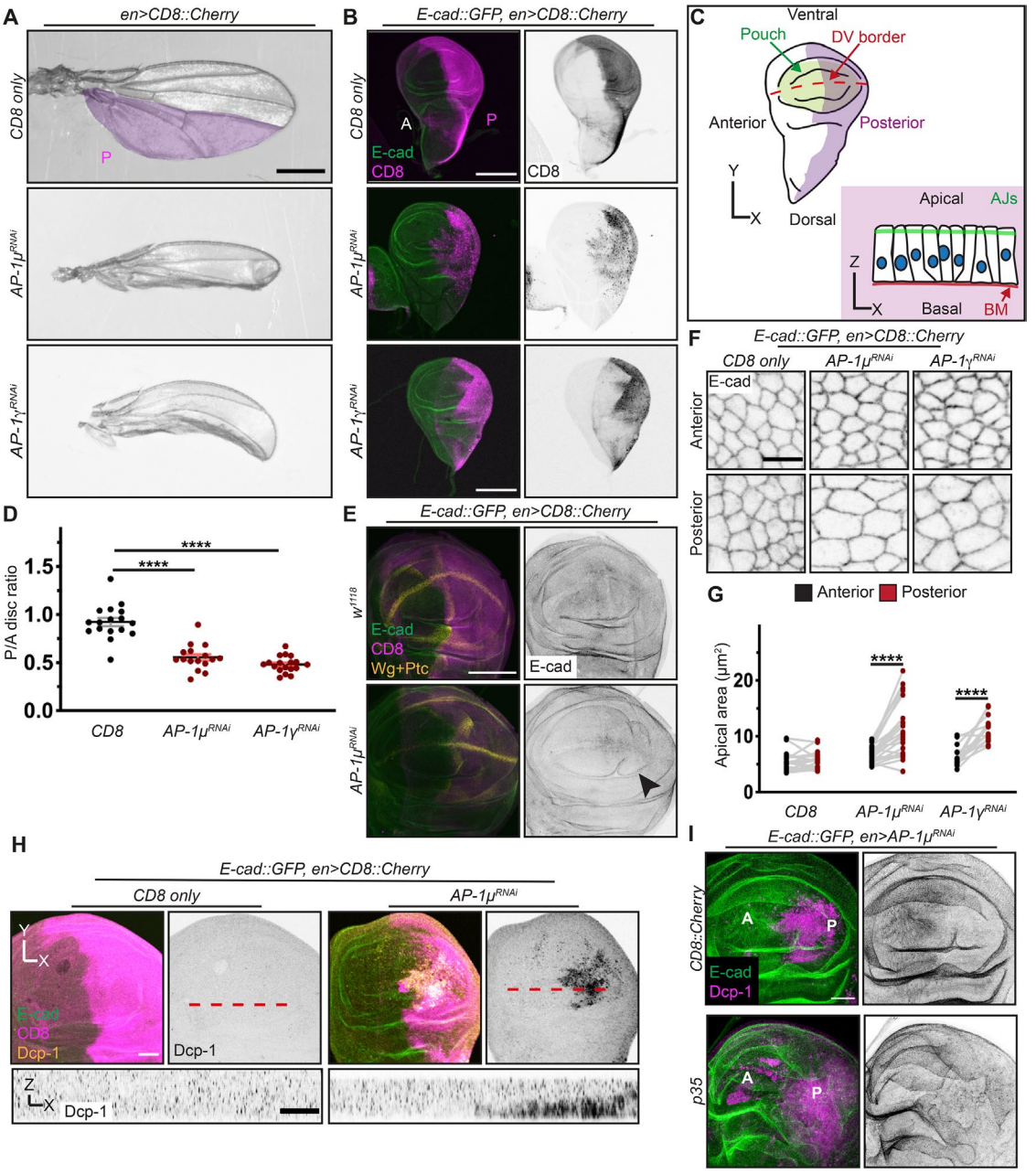

FIGURE 1: AP-1 regulates development, cell morphology, and survival in the wing disc. (A) Wings expressing CD8::Cherry alone or with AP-1 RNAi in the posterior compartment. Scale bar: 0.5 mm. (B) Wing discs expressing CD8::Cherry (magenta, left; grayscale, right) alone or with AP-1 RNAi, showing E-cad::GFP (green, left) and anterior (A) and posterior (P) compartments. Scale bar: 150 μm. (C) Top; cartoon view of a wing imaginal disc with posterior compartment (magenta), wing pouch (green), and dorsoventral border (DV, dashed red line). Bottom: sagittal view of the wing pouch epithelium with the AJs (green) and the basal membrane (BM, red). (D) P:A area ratios of control and AP-1 RNAi-expressing discs. Dots represent individual discs ($n = 17$, 16, and 18). ****$p < 0.0001$ (Brown-Forsythe and Welch ANOVA test). (E) Wing pouches expressing CD8::Cherry alone or with AP-1μ RNAi, costained for Wingless and Patched (Wg and Ptc, both in yellow). E-cad::GFP visualizes the tissue architecture (green, left; grayscale, right). Arrowhead indicates an ectopic fold. Scale bar: 100 μm. (F) Dorsal wing pouch cells expressing *shg*-E-cad::GFP (grayscale) in the indicated compartments (rows) and genotypes (columns). Scale bar: 5 μm. (G) Cell apical area of wing pouch cells. Each dot represents the average of an individual disc ($n = 15$–23 discs/genotype). ****$p < 0.0001$ (two-way ANOVA). (H) Wing pouches expressing CD8::Cherry alone or with AP-1μ RNAi with E-cad::GFP (green, left), CD8::Cherry (magenta, left) and cleaved effector caspase (Dcp-1, yellow, left; grayscale, right and bottom sagittal projection of the dashed line). Scale bars: 50 μm (top) and 20 μm (bottom). (I) Wing pouch regions of discs expressing AP-1μ RNAi with CD8::Cherry (top, not shown) or p35 (bottom) in the posterior compartment visualized with E-cad::GFP (green, left; inverted grayscale, right) and cleaved caspase-3 (DCP-1, magenta, left). Anterior (A) and posterior (P) compartments are indicated. Scale bar: 50 μm.

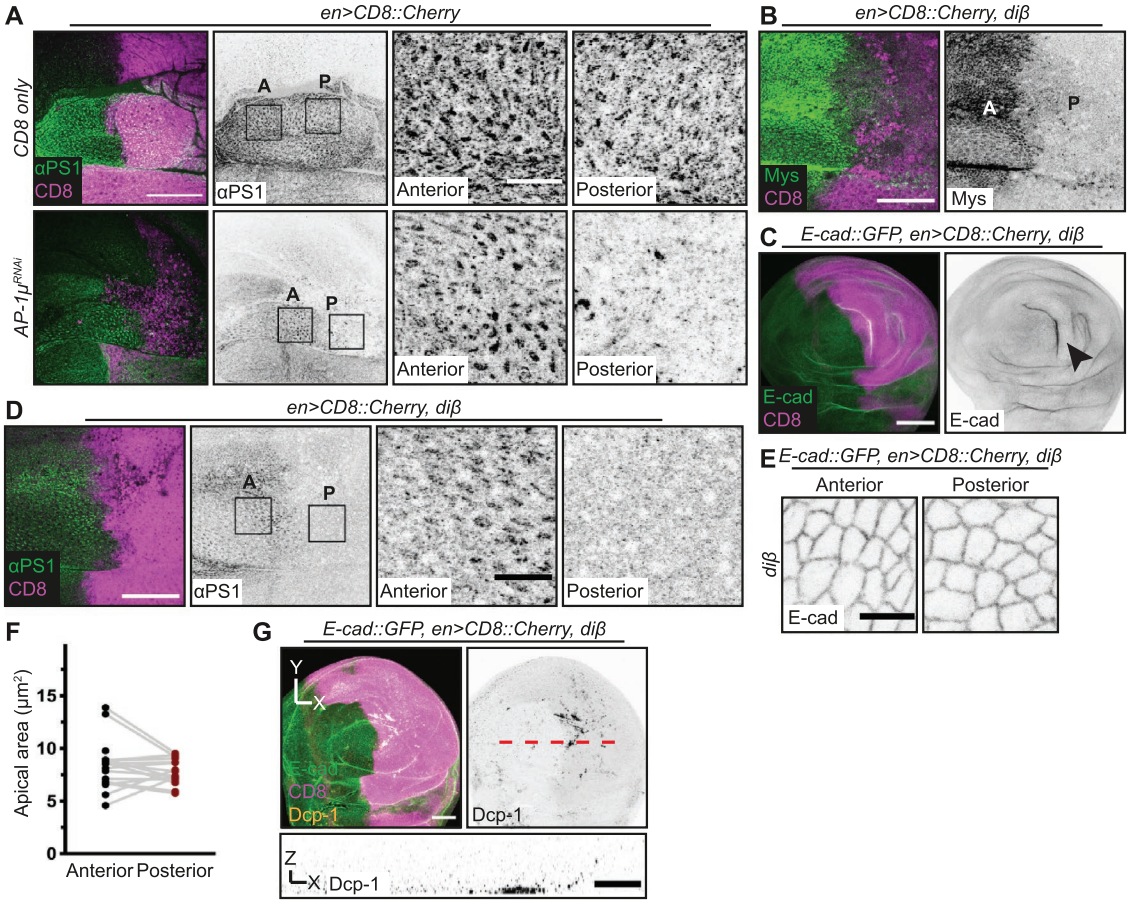

FIGURE 2: Disruption of basal polarity is not responsible for the AP-1 knockdown phenotype. (A) Basal region of wing discs expressing CD8::Cherry alone or with AP-1μ RNAi, costained with αPS1 (green, left; grayscale, right). Anterior (A) and posterior (P) compartment areas (right panels) are highlighted by rectangles (left). Scale bars: 50 μm (left); 10 μm (right). (B) Basal region of wing disc expressing CD8::Cherry (magenta, left) and diβ, stained for βPS integrin (Mys, green, left; inverted grayscale, right) and confirming the displacement of the endogenous βPS. Areas in the anterior (A) and posterior (P) compartments are indicated. Scale bar: 50 μm. (C) Wing pouch regions of discs expressing CD8::Cherry protein (magenta, left) with diβ in the posterior compartment. E-cad::GFP is shown to visualize tissue architecture (green, left; inverted grayscale, right). Arrowhead indicates an ectopic fold. Scale bar: 100 μm. (D) Basal region of wing discs expressing CD8::Cherry with diβ, stained with αPS1 integrin (green, left; grayscale, right). Areas in the anterior (A) and posterior (P) compartments (right panels) are highlighted by rectangles (left). Scale bars: 50 μm (left); 10 μm (right). (E) Dorsal wing pouch cells expressing *shg*-E-cad::GFP (grayscale) expressing CD8::Cherry with diβ in the posterior compartment. Scale bar: 5 μm. (F) Cell apical area of discs depicted in E. Each dot represents the average of an individual disc; compartments from the same disc are connected by gray lines ($n = 22$ discs). (G) Wing pouches expressing CD8::Cherry with diβ, visualized with E-cad::GFP (green, left), CD8::Cherry (magenta, left), and cleaved effector caspase (Dcp-1, yellow, left; grayscale, right and bottom sagittal projection of the dashed line). Scale bars: 50 μm (top) and 20 μm (bottom).

the wing disc AJs (Figure 3, A–C), as well as in the embryonic epidermis and pupal eyes (Supplemental Figure S3, A and B). In contrast, we detected only a few puncta at the basal surface, with no αPS1 colocalization (Figure 3A and Supplemental Figure S3, C and D). AP-1γ knockdown reduced levels of AP-1μ::VFP in the cytoplasm and at AJs (Figure 3, D–F), which we measured as either the mean intensity of native VFP fluorescence or its total content to account for the increased apical perimeter. These results suggested that the AP-1μ::VFP assembles into the AP-1 complex at AJs as well as in the cytoplasm. Indeed, we observed a colocalization at AJs between E-cad::GFP and an AP-1γ antibody (Supplemental Figure S3, E and F) (Benhra *et al.*, 2011).

To explore the roles of the AP-1 complex at AJs, we analyzed the distribution and levels of E-cad. The mean levels of *shg*-E-cad::GFP at AJs were mildly reduced, while the total junctional protein content was unchanged or mildly elevated following AP-1 knockdown (Figure 4, A–C). At the same time, we observed intracellular vesicles containing *shg*-E-cad::GFP, which are rarely seen in the control (Figure 4. A and B). To examine whether AP-1 knockdown led to the accumulation of E-cad intracellularly, we measured the cytoplasmic intensity of *shg*-E-cad::GFP in the plane of AJs ("subapical cytoplasm" hereafter). Although it does not include all of the cytoplasm, both TGN and REs are found in this region (Supplemental Figure S4) and the signal can be confidently attributed to individual cells. The mean levels of *shg*-E-cad::GFP in the subapical cytoplasm were also mildly reduced (Figure 4C). However, when normalized to the increase in the apical cell area, the total subapical intracellular content of *shg*-E-cad::GFP was elevated, in agreement with the observed increase of E-cad–containing puncta (Figure 4D). Therefore, AP-1 knockdown elevated the ratio of *shg*-E-cad::GFP content in the

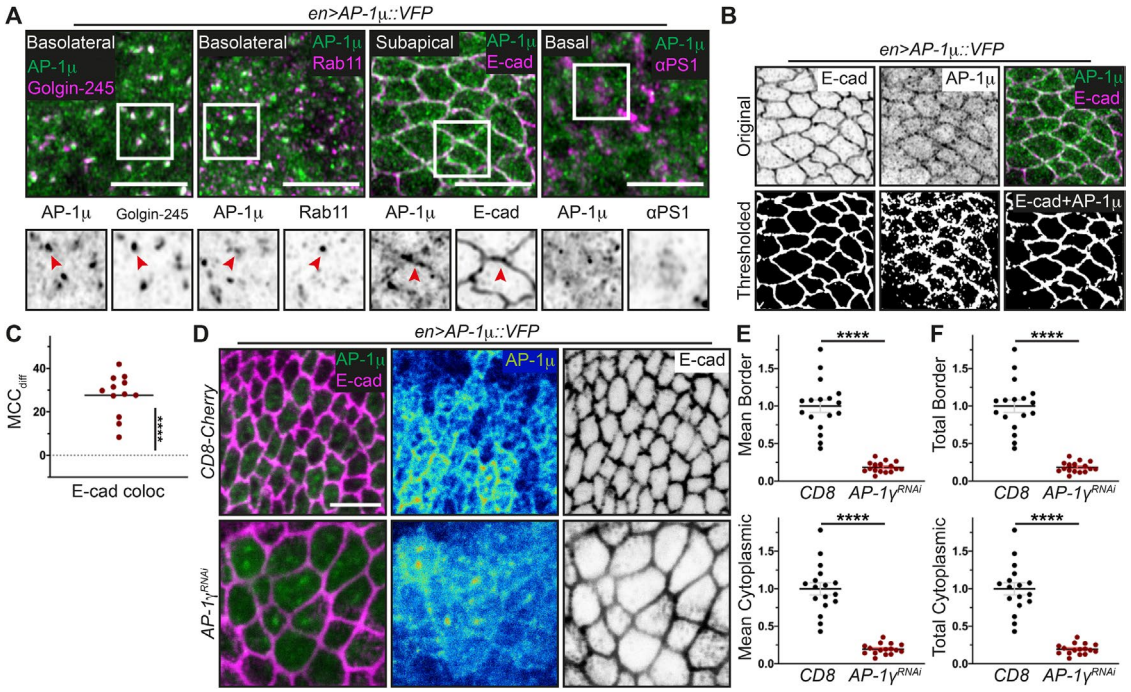

FIGURE 3: AP-1 displays an apical pool colocalizing with E-cad. (A) Average projections of the posterior compartments of wing discs expressing AP-1μ::VFP (green) and costained with markers (magenta) of the TGN (Golgin-245), REs (Rab11), the AJs (E-cad), and the basal membrane (integrin αPS1). Grayscale images correspond to AP-1μ::VFP and each marker within the white square on the image above, with red arrowheads indicating colocalization. Scale bar: 5 μm. (B) Detail of the colocalization between E-cad antibody (inverted grayscale, top left; magenta, top right) and AP-1μ::VFP (inverted grayscale, top center; green, top right), as shown originally in A. Bottom panels depict automatic thresholded images (left and center) and the pixels that are positive for both thresholded channels (bottom right). (C) MCC_{diff} (see *Materials and Methods*) for the E-cad and AP-1μ::VFP signals ($n = 12$, sections = 6 per sample). ****$p < 0.0001$ (one-sample *t* test in comparison to zero for random colocalization). (D) Posterior compartments of wing discs expressing AP-1μ::VFP (green, left; heatmap, right) together with CD8::Cherry (unpublished, top) or AP-1γ RNAi (bottom) costained for E-cad (magenta, left; grayscale, right). Scale bar: 5 μm. (E, F) Mean (E) and total (F) AP-1μ::VFP levels at the cell borders (top) and in the cytoplasm (bottom). Each dot represents average for an individual disc ($n = 17, 16$). ****$p < 0.0001$ (two-tailed *t* test).

subapical cytoplasm relative to the plasma membrane (Figure 4E). Additionally, an increase in the cytoplasmic content combined with no change in the junctional *shg*-E-cad::GFP may indicate an increase in the total amount of protein per cell, which could be due to either elevated protein production or reduced degradation. We tested whether there were changes in the protein production and found that AP-1 knockdown indeed increased *shg* mRNA levels (Figure 4F).

To exclude the effects of AP-1 knockdown on *shg* gene expression, we used the GFP-tagged E-cad expressed from the ubiquitous *Ubi-p63E* promoter (*ubi*-E-cad::GFP; Figure 5A [Oda and Tsukita, 2001]). The levels of *ubi*-E-cad::GFP were slightly lower than those of *shg*-E-cad::GFP (Figure 5, E and F, and Supplemental Figure S5), suggesting physiological levels of E-cad in these cells in the control. We confirmed that the levels of *ubi*-E-cad::GFP protein were insensitive to *shg* mRNA expression by measuring them in the presence of the loss-of-function shg^{IG27} allele (Warrington *et al.*, 2013). In agreement with our recent findings of a feedback loop that stabilizes the levels of E-cad in wing discs (Ramirez Moreno *et al.*, 2021), levels of *shg*-E-cad::GFP increased to compensate for the absence of the second gene copy (Figure 5, E and F, and Supplemental Figure S5, A–C). However, levels of *ubi*-E-cad::GFP were not increased by the shg^{IG27} allele (Figure 5, E and F, and Supplemental Figure S5, A–C). At the same time, we observed that the down-regulation of both μ and γ AP-1 subunits halved the mean *ubi*-E-cad::GFP levels at the AJs and also reduced the total levels (Figure 5, A–C) (Wu and Pollard, 2005; Coffman and Wu, 2012). Concurrently, while the mean signal of *ubi*-E-cad::GFP in the subapical cytoplasm was also reduced, the total subapical intracellular content remained normal or even slightly increased as a consequence of the increased apical cell area (Figure 5, B and C). Therefore, for *ubi*-E-cad::GFP, AP-1 knockdown also elevated the ratio of its content in the subapical cytoplasm relative to the plasma membrane (Figure 5D). The changes of the *ubi*-E-cad::GFP levels and cytoplasm/junction ratio were not rescued by inhibiting apoptosis using p35 expression (Supplemental Figure S5, E–H), confirming that it is not a consequence of cell death.

The increase in the relative level of E-cad in the cytoplasm at the level of AJs and the intracellular puncta observed for *shg*-E-cad::GFP indicated E-cad accumulation in one or several intracellular compartments. Owing to the localization of the AP-1 complex at the TGN and REs, we examined colocalization of both E-cad::GFP proteins with these compartments in the subapical cytoplasm and found that AP-1μ knockdown increased the colocalization in all cases (Figure 6, A–F). We also found a lack of colocalization of E-cad::GFP proteins with the Golgi bodies in the controls, which is indicative of a very low residency time of E-cad::GFP there in the control. The colocalization was, however, noticeable and significantly above zero following AP-1 knockdown (Figure 6, C and F).

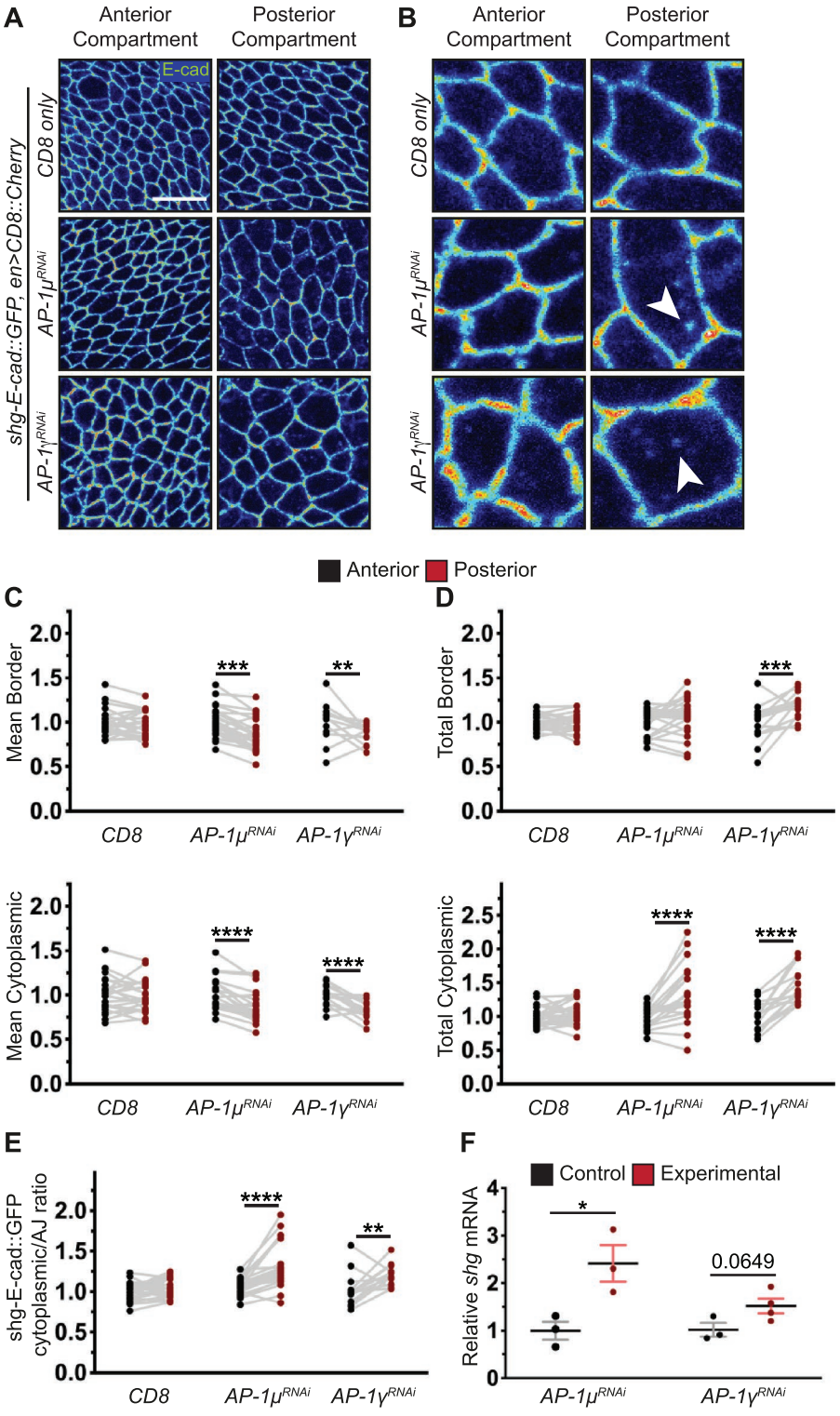

FIGURE 4: AP-1 controls the levels and expression of E-cad. (A) Dorsal wing disc pouch cells expressing *shg*-E-cad::GFP (heatmap) in the indicated compartments (columns) and genotypes (rows). Scale bar: 10 μm. (B) Detail of the panels in A. White arrowheads indicate intracellular E-cad::GFP accumulation. (C, D) Mean (C) and total (D) *shg*-E-cad::GFP protein levels at the cell borders (top) and in the cytoplasm (bottom). (E) Cytoplasm/AJ ratio of *shg*-E-cad::GFP total levels. (F) *shg* expression levels in control and with AP-1 subunits knockdown. On all graphs, dots represent individual discs ($n = 22, 23, 15$), apart from F, where each dot is an independent biological replicate ($n = 3, 3, 3$, and 4 per genotype); data from the same discs are connected by gray lines. *$p < 0.05$, **$p < 0.01$, ***$p < 0.001$, and ****$p < 0.0001$. Two-way ANOVA in C–E; Welch's *t* test in F.

A decrease in the plasma membrane levels and increase of the relative intracellular accumulation of *ubi*-E-cad::GFP could be due to either elevated protein internalization from the surface, its retention within intracellular compartments, or a combination of both. As we found a pool of AP-1 colocalizing with E-cad at AJs, we focused on testing the potential role for AP-1 in E-cad internalization from the plasma membrane. We used fluorescence recovery after photobleaching (FRAP) to measure the dynamics of the *ubi*-E-cad::GFP at the AJs (Figure 7, A and B). E-cad recovery in FRAP is diffusion-uncoupled and best-described by a biexponential model with the slow component mediated by endocytic recycling (Bulgakova *et al.*, 2013; Bulgakova and Brown, 2016; Iyer *et al.*, 2019). We found that AP-1 depletion halved the halftime of the slow component's recovery (Figure 7B). E-cad recovery following AP-1 depletion was best-fitted by a single exponential model, likely as the slow halftime reduction made it impossible to confidently separate the components (Greig and Bulgakova, 2021). The halftime of a diffusion-uncoupled recovery depends only on the reaction off-rate (internalization rate in this case) (Sprague and McNally, 2005; Iyer *et al.*, 2019): smaller halftime means larger off-rate. Therefore, we conclude that E-cad internalization from AJs is elevated upon AP-1 knockdown, which is consistent with AP-1 acting on endocytosis at AJs. We, however, cannot exclude that this elevated internalization is not accompanied by the retention of E-cad within intracellular compartments.

Next, we validated the increased endocytic internalization of E-cad from the plasma membrane with the pulse-chase assay (Figure 7C). We measured the internalization of an antibody against the E-cad extracellular domain bound to E-cad at the cell surface as a readout of the E-cad endocytosis from the membrane (Figure 7D) (Bulgakova and Brown, 2016). In this instance, we measured E-cad-antibody–containing puncta just below the AJ belt to confidently exclude the signal coming from the plasma membrane while remaining within the area rich in the TGN and RE signal (Supplemental Figure S4). We found that the number of vesicles containing E-cad antibody doubled following AP-1μ knockdown at 30 and 60 min after labeling (Figure 7E). As expected, this internalized E-cad colocalized with TGN in both the control and AP-1–depleted cells (Figure 7, F and G).

We finally asked whether the elevated cytoplasmic E-cad and its cytoplasm/AJ ratios were responsible for apoptosis following AP-1 knockdown (Figure 1H), as in the wing discs the failure to localize E-cad at AJs induces

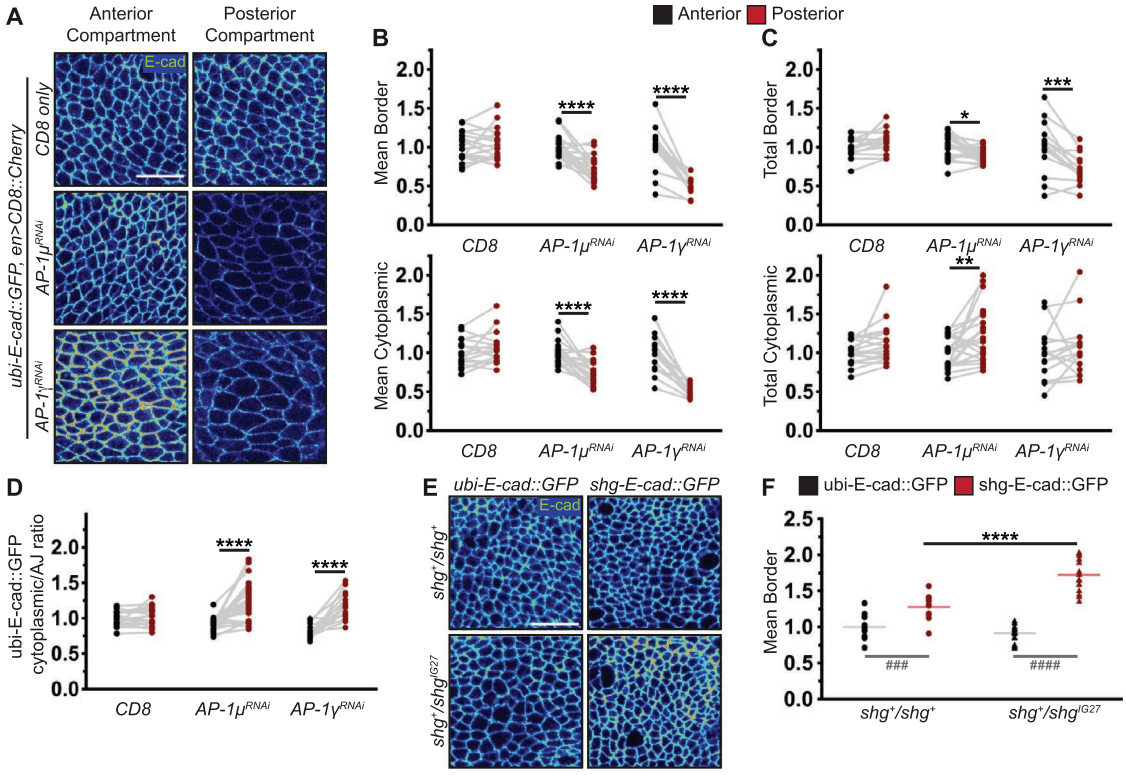

FIGURE 5: AP-1 controls the levels and expression of E-cad (cont.). (A) Dorsal wing pouch cells expressing *ubi*-E-cad::GFP (heatmap) in the indicated compartments (columns) and genotypes (rows). Scale bar: 10 μm. (B, C) Mean (B) and total (C) *ubi*-E-cad::GFP levels at the cell borders (top) and in the cytoplasm (bottom). (D) Cytoplasm/AJ ratio of the total levels for *ubi*-E-cad::GFP. (E) Dorsal wing pouch cells expressing E-cad::GFP (heatmap) with the indicated constructs (columns) in the different genotypes (rows). Scale bar: 10 μm. (F) Mean E-cad::GFP levels at the cell borders as depicted in E. On all graphs, dots represent individual discs, (n = 17, 23, 15 in B–D and 14, 13, 14, 14 in F); data from the same discs are connected by gray lines in B–D. *$p < 0.05$, **$p < 0.01$, ***$p < 0.001$, and ****$p < 0.0001$ (two-way ANOVA in B–D, F). ###$p < 0.001$ and ####$p < 0.0001$ (two-way ANOVA in F).

apoptosis through activation of JNK signaling (Jezowska *et al.*, 2011). Indeed, using an antibody against phosphorylated JNK (pJNK), we found that JNK signaling was elevated following AP-1μ knockdown (Figure 8, A and B). Up-regulation of pJNK was more pronounced when apoptosis was inhibited with p35 overexpression (Figure 8C), in agreement with the intense activation of JNK signaling in tissues with undying cells (Pérez-Garijo *et al.*, 2009). We examined whether inhibiting E-cad endocytosis ameliorated the phenotype that we observed upon AP-1 knockdown. To specifically block endocytosis of E-cad without effects on general endocytic machinery, we overexpressed p120-catenin, which directly binds the E-cad intracellular domain and prevents its internalization in both flies and mammalian cells (Xiao *et al.*, 2007; Iyer *et al.*, 2019; Greig and Bulgakova, 2020b). We confirmed that p120-catenin overexpression increased the stable fraction of E-cad at the membrane, in agreement with its effect in the embryonic epidermal cells (Figure 8, D and E) (Greig and Bulgakova, 2020b). While overexpression of p120-catenin did not affect wing size by itself, coexpression of p120-catenin with AP-1μ RNAi increased the wing size relative to AP-1 knockdown, indicating a partial rescue (Figure 8, F and G). To determine the cause of this rescue, we examined cell death and integrin localization in wing discs coexpressing p120-catenin with AP-1μ RNAi. There was no difference in αPS1 integrin localization with or without p120-catenin overexpression in wing discs expressing AP-1μ RNAi (Figure 8H), which was consistent with wing blisters observed in wings coexpressing p120-catenin with AP-1μ RNAi (Figure 8F). However, there was less cell death visualized using Dcp-1 antibody in wing discs that overexpressed p120-catenin than in those that did not upon AP-1μ knockdown (Figure 8, I and J). Therefore, we conclude that reducing E-cad endocytosis in AP-1–depleted cells prevents cell death, suggesting that elevated E-cad endocytosis contributed to cell death induction upon AP-1 down-regulation (Figure 9B).

DISCUSSION

In this study, we report complex morphological changes caused by the reduced function of the AP-1 complex. While such a pleiotropic effect is expected from proteins with a general role in intracellular trafficking, the reported phenotypes are very specific and can be attributed to a limited number of specific cargoes, for example, the ectopic folding is consistent with the defects in basal targeting of integrins. Concurrently, the elevated level of cell death can be attributed to hyperinternalization of E-cad from the cell surface as it was reduced by inhibiting E-cad endocytosis (Figure 8, I and J). Such an effect of AP-1 down-regulation on E-cad at the cell surface was rather unexpected but does agree with the colocalization of a distinct subapical AP-1 pool with AJs that we report. Finally, we found that this hyperinternalization of E-cad was accompanied by increased E-cad expression, compensating for the loss of E-cad at the plasma membrane (Figures 4F and 9A).

While localization of AP-1 at AJs was not previously reported, it is not surprising as AP-1 has been found at the plasma membrane in

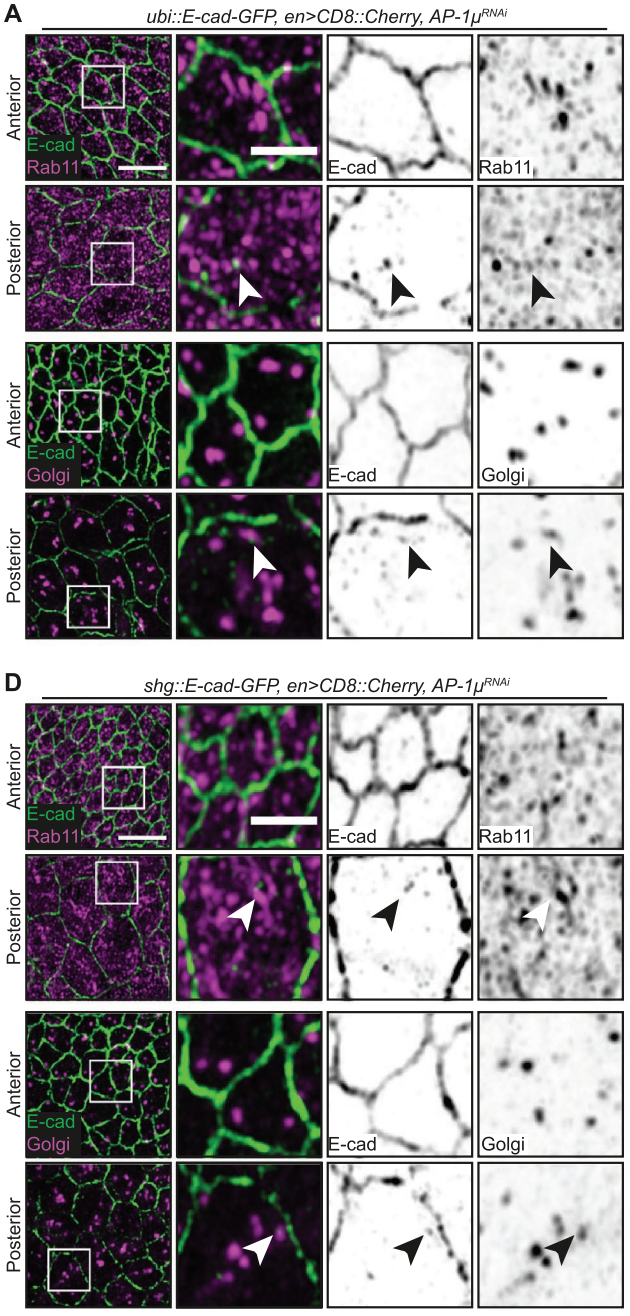

FIGURE 6: AP-1 knockdown increases the intracellular pool of E-cad. (A) Dorsal wing pouch regions of discs coexpressing *ubi-E-cad::GFP* (green) with CD8::Cherry (not shown) and AP-1μ RNAi in the posterior compartment. Discs are stained for Rab11 (top two rows) and Golgi mab (bottom two rows), both depicted in magenta. Right panels show magnified regions within the white squares in left panels. Arrowheads indicate colocalization of E-cad and each marker. Scale bars: 5 μm (left) and 2 μm (detail). (B) MCC_{diff} (see *Materials and Methods*) for the colocalization between Rab11 and *ubi-E-cad::GFP*. Each dot represents the average for individual paired compartments ($n = 20$ discs, sections = 10 per disc). *$p < 0.05$ (Wilcoxon test); **$p < 0.01$, and ***$p < 0.001$ (one-sample *t* test). (C) MCC_{diff} (see *Materials and Methods*) for the colocalization between Golgi and *ubi-E-cad::GFP*. Each dot represents the average for individual paired compartments ($n = 15$ discs, sections = 10 per disc). ***$p < 0.05$ (Wilcoxon test and one-sample *t* test); *$p < 0.01$ and ***$p < 0.001$ (one-sample *t* test). (D) Dorsal wing pouch regions of discs coexpressing *shg-E-cad::GFP* (green) with CD8::Cherry (not shown) and AP-1μ RNAi in the posterior compartment. Discs are stained for Rab11 (top two rows) and Golgi mab (bottom two rows), both depicted in magenta. Right panels show magnified regions within the white squares in the left panels. Arrowheads indicate colocalization of E-cad and each marker. Scale bars: 5 μm (left) and 2 μm (detail). (E) MCC_{diff} (see *Materials and Methods*) for the colocalization between Rab11 and *shg-E-cad::GFP*. Each dot represents the average for individual paired compartments ($n = 14$ discs, sections = 10 per disc). *$p < 0.05$ (one-sample *t* test) and **$p < 0.01$ (Wilcoxon test). (F) MCC_{diff} (see *Materials and Methods*) for the colocalization between Golgi and *shg-E-cad::GFP*. Each dot represents the average for individual paired compartments ($n = 17$ discs, sections = 10 per disc). *$p < 0.05$ (one-sample *t* test) and **$p < 0.01$ (Wilcoxon test and one-sample *t* test).

such diverse systems as the cell–extracellular matrix adhesion in mammalian kidney cells and phagosomes in *Dictyostelium* amoebas (Lefkir *et al.*, 2004; Kell *et al.*, 2020). Additionally, both Arf1 and Arf6—two small GTPases that contributed to the recruitment of AP-1A and AP-1B, respectively, in mammalian cells—are found at the plasma membrane, where they regulate endocytosis in both fly and mammalian cells (Stamnes and Rothman, 1993; D'Souza-Schorey *et al.*, 1995; Kumari and Mayor, 2008; Shteyn *et al.*, 2011; Sauvageau *et al.*, 2017; Greig and Bulgakova, 2020a,b). Moreover, Arf1 and AP-1 share the localization pattern being present at both TGN and AJs. Their involvement in both endocytosis and delivery to the plasma membrane provides a potential mechanism for integration of these processes, whereby changes in one lead to fine-tuning of the other. The coupling of exocytosis and compensatory endocytosis is established in neuronal cells, where SNARE-proteins and Ca^{2+} concentrations adjust the balance between two processes. To understand the consequences of such coupling, it would be important to determine proteins whose trafficking is affected by each pool of AP-1 and whether both pools act on the same proteins. However, dissecting the functions of individual pools is challenging. For example, while we established that knockdown of AP-1 promotes E-cad endocytosis, we cannot exclude that the retention of E-cad at the REs/TGN contributes to phenotype, as AP-1B is required for E-cad delivery to the plasma membrane in mammalian cells (Ling *et al.*, 2007).

Intriguingly, E-cad endocytosis was enhanced upon the loss of AP-1, as it is a trafficking adaptor usually thought to promote vesicular transport. Similarly, in mammalian cells (LLC-PK1), expression of AP-1B slowed cell migration, which is consistent with the reduced integrin turnover (Palamidessi *et al.*, 2013; Kell *et al.*, 2020). One of the scenarios proposed for the AP-1B function at the plasma membrane in these cells was that AP-1B forms coats that abort without scission but at the same time occupy binding

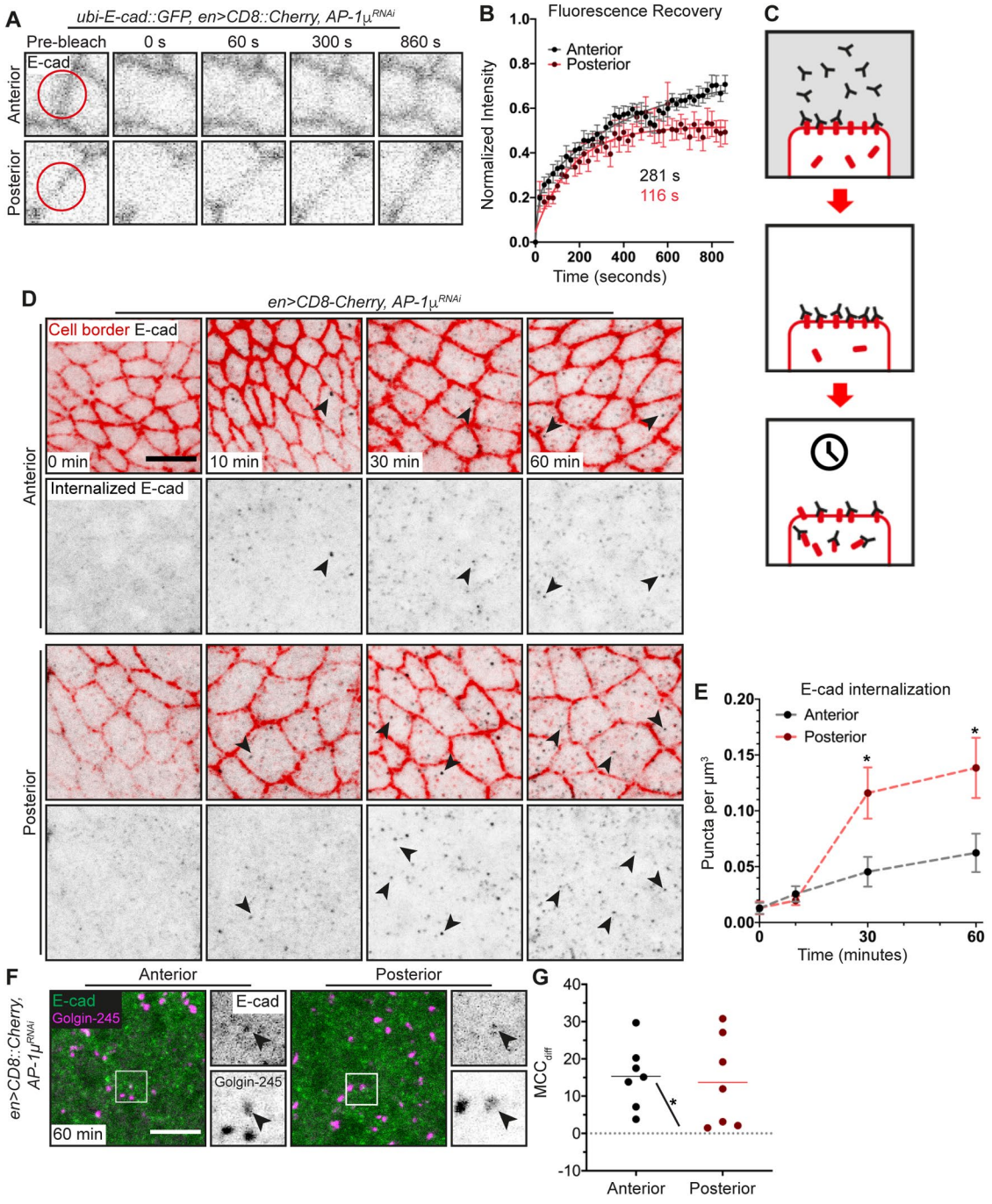

FIGURE 7: AP-1 decelerates E-cad endocytosis. (A) Frames of *ubi*-E-cad::GFP FRAP at wing disc cell borders at the indicated compartments and time points. Red circles in prebleached frame (P) outline the bleached spots. (B) Average recovery curves (mean ± SEM, $n = 16$ and 15 cells from seven wing discs), with the best-fit curves (solid lines) and slow halftimes. (C) Cartoon depicting the pulse-chase protocol to measure uptake of E-cad antibody. (D) Pulse-chase labeling with E-cad antibody in the anterior (control) and posterior (expressing AP-1μ RNAi) compartments of wing discs. Apical region with AJs is in red; the puncta (examples indicated with arrowheads) in the 1.9 μm below in black. Scale bar: 5 μm. (E) The number of vesicles per μm^3 during pulse-chase labeling (mean ± SEM, $n = 5–7$ compartments/time point). *$p <$ 0.05 (Welch's *t* test). (F) Pulse-chase labeling (60 min) with E-cad antibody (green, left) and stained for Golgin-245 (magenta, left), in the anterior (control) and posterior (expressing AP-1μ RNAi) compartments of a wing disc. Grayscale images correspond to E-cad (top) and Golgin-245 (bottom) signal within the white square on the left image. Scale bar: 5 μm. (G) MCC_{diff} (see *Materials and Methods*) for the colocalization between internalized E-cad antibody and Golgin-245. Each dot represents the average for individual paired compartments ($n = 7$ discs). *$p < 0.05$ (Wilcoxon signed-rank test).

sites for AP-2 and thus reduce the net rate of AP-2–mediated endocytosis. Alternatively, both AP-1 and AP-2 may be involved in E-cad endocytosis, but clathrin-coated pits mature faster in the case of AP-2 recruitment due to the presence of specific modifying enzymes such as kinases, which can alter the speed of maturation (Wrobel *et al.*, 2019). Then in the absence of AP-1, the remaining AP-2–driven

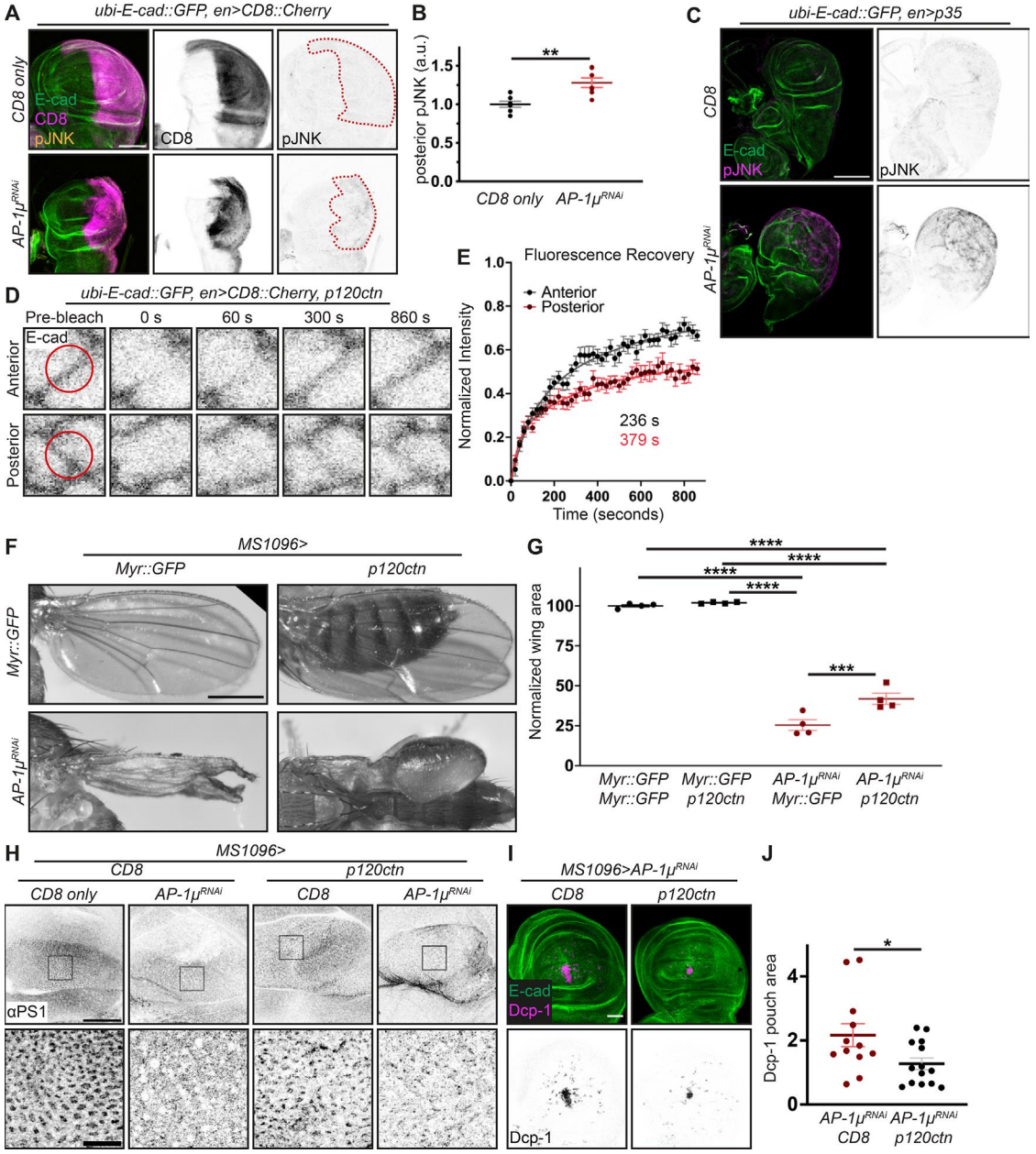

FIGURE 8: AP-1 promotes cell survival by controlling intracellular levels of E-cad. (A) Wing pouch regions of discs expressing CD8::Cherry (magenta, left; inverted grayscale, middle) alone (top) or with AP-1μ RNAi (bottom), showing ubi-E-cad::GFP (green, left) and phosphorylated JNK (pJNK, yellow, left; inverted grayscale, right). Dashed red lines in pJNK panels indicate the posterior compartment of the pouch as identified by CD8::Cherry. Scale bar: 100 μm. (B) Relative intensity (normalized with control) of pJNK antibody at the posterior compartments depicted in A ($n = 7$ discs per genotype). $^{**}p < 0.01$ (unpaired t test). (C) Wing discs expressing p35 protein with CD8::Cherry (not shown, top) or with AP-1μ RNAi (bottom) at the posterior compartment, showing E-cad::GFP (green, left), and phosphorylated JNK (pJNK, magenta, left; inverted grayscale, right). Scale bar: 150 μm. (D) *ubi*-E-cad::GFP FRAP at wing disc cell borders at the indicated compartments and time points. Red circles in prebleached frame (P) outline the bleached spots. (E) Average recovery curves (mean ± SEM, $n = 34$ and 24 cells, from nine wing discs), with the best-fit curves (solid lines) and slow halftimes. (F) Adult wings expressing the indicated proteins or AP-1μ RNAi in their wing pouches. Scale bar: 0.5 mm. (G) Relative area (normalized to Myr::GFP controls) of adult female wings depicted in A. Dots represent individual adults ($n = 4$ per genotype). $^{***}p < 0.001$ and $^{****}p < 0.0001$ (Brown-Forsythe and Welch ANOVA test). (H) Basal region of wing discs expressing either CD8::Cherry or AP-1μ RNAi together with CD8::Cherry (a single copy in the case of CD8::Cherry) or p120ctn, stained for αPS1 (grayscale) with regions highlighted by rectangles shown in the bottom row. Scale bars: 50 μm (top); 10 μm (bottom). (I) Wing pouch regions of discs expressing AP-1μ RNAi with CD8::Cherry (left, not shown) or p120ctn (right) in the posterior compartment visualized with E-cad antibody (green, top) and cleaved caspase-3 (Dcp-1, magenta, top; inverted grayscale, bottom). Scale bar: 50 μm. (J) Percentage of wing pouch region occupied by Dcp-1 signal. Dots represent individual discs for each genotype ($n = 12$ and 14). $^{*}p < 0.05$ (unpaired t test).

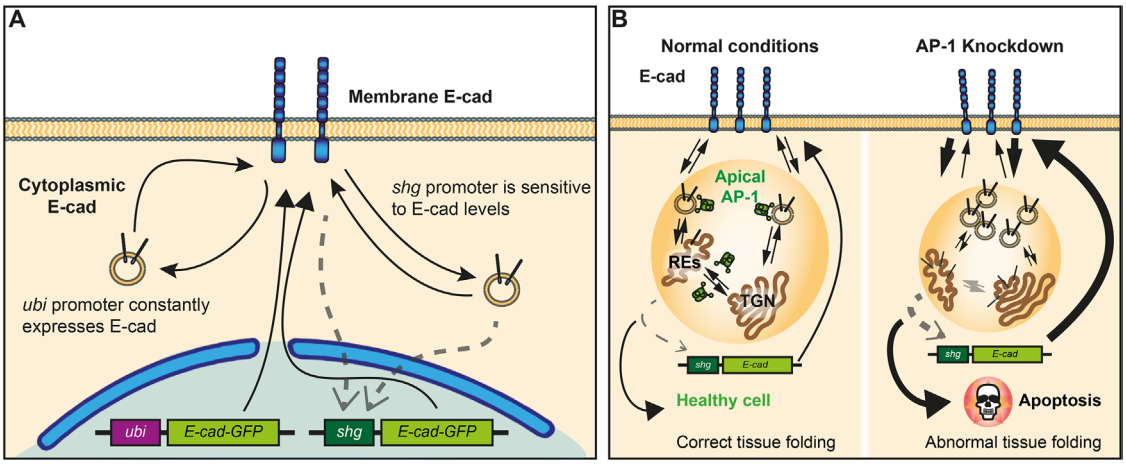

FIGURE 9: Summary models. (A) Model of the proposed E-cad feedback. The cytoplasmic/AJ ratio of E-cad influences the transcription of the *shg* gene. Only the endogenous *shg*-E-cad::GFP is affected by this. (B) Model of the functions of AP-1 in the developing wing discs. In control (left), besides vesicle trafficking between the REs and the TGN, a subapical fraction of AP-1 localizes at/near the AJs. Upon AP-1 knockdown (right), E-cad is retained in TGN/REs following its elevated endocytosis from the AJs and possibly delayed delivery to the AJs. This increase of E-cad intracellular levels induces cell death. To bring E-cad membrane levels back to normal, cells increase *shg* expression.

endocytosis would lead to the faster net rate of E-cad internalization. In either scenario, it makes physiological sense that AP-1 slows E-cad internalization from AJs. If there is a limited common pool of AP-1, its reduced localization to TGN would potentially lead to increased AP-1 availability for recruitment to AJs. Such reduced localization of AP-1 to TGN could be a consequence of impairment in TGN function and a sign of reduced E-cad delivery to the plasma membrane. In this case, the concurrent elevation of AP-1 at AJs will reduce E-cad removal from the plasma membrane, thus restoring E-cad levels at AJs and contributing to adhesion robustness.

Such robustness of adhesion is further supported by our observation of increased *shg* expression upon AP-1 knockdown (Figure 4F), suggesting the existence of a feedback loop. We have recently reported feedback between E-cad protein levels and its gene expression; specifically, the recruitment of the transcription regulator STAT92E to E-cad adhesion via the Par-3 protein limits its availability for binding the Heterochromatin Protein 1 (HP-1) in the nucleus (Ramirez Moreno *et al.*, 2021). This mechanism allows restoring E-cad expression when its levels are altered; elevated E-cad leads to reduced nuclear STAT92E and hence, HP-1 function, which reduces not only heterochromatin formation but also E-cad expression. Increased *shg* expression in cells lacking AP-1 suggests that this feedback mechanism might be activated not only by the total E-cad protein level but also by the enhanced internalization of E-cad from the cell surface and retention of this internalized E-cad at TGN/REs (Figure 9A).

In addition to promoting *shg* expression, we found that the relative increase of intracellular E-cad compared with the membrane pool induced cell death. This is consistent with the observed upregulation of the JNK signaling and the reported JNK-mediated apoptosis upon mislocalization of E-cad to AJs in cells mutant for actin capping protein, accompanied by overproliferation upon apoptosis inhibition (Jezowska *et al.*, 2011). It is worth mentioning that the loss of the capping protein also leads to increased E-cad expression, supporting the feedback mechanisms described above. Similarly, we observed hyperplastic overgrowth of wing discs when apoptosis was inhibited upon AP-1 knockdown (Figure 1H). Therefore, apoptosis induction following E-cad hyperinternalization may provide a protective mechanism whereby defective cells are eliminated (Figure 9B). This mechanism agrees well with the multistage theory of cancerogenesis (Weiss, 2004), so that additional sequential mutations are required to overcome both this cell-death–inducing mechanism and the feedback that restores E-cad levels.

In summary, we provide evidence that a subapical pool of the AP-1 complex exerts a brake upon E-cad internalization, excess of which promotes cell death. We demonstrate that this AP-1 function is accompanied by transcriptional feedback, which maintains E-cad levels at the cell surface. In line with the correlation of the AP-1B loss with the metastatic potential in humans (Kell *et al.*, 2020), our findings highlight the pivotal role of the AP-1 complex in preventing tumor progression and enabling correct epithelial morphogenesis.

MATERIALS AND METHODS

Request a protocol through *Bio-protocol*.

Fly genetics and husbandry

Drosophila melanogaster flies were raised on standard cornmeal/agar/molasses media at 18°C or 25°C unless otherwise specified. To express constructs of interest, the GAL4/UAS system was used (Brand and Perrimon, 1993), with *engrailed*-GAL4 (*en*-GAL4), *MS1096*-GAL4, or *Act5C*-GAL4 drivers. To examine adult wings, flies were raised at 18°C to circumvent potential lethality due to RNAi expression. To study larval wing discs, larvae were raised at 25°C. The GAL4:UAS ratio was kept constant within each experimental data set using additional copies of *UAS*-CD8::Cherry or *UAS*-myristoylated::GFP (*UAS*-myr::GFP). Acute expression of RNAi was achieved with the combination of *Act5C*-GAL4 and *tubulin*-GAL80^{ts}. Larvae then were raised at 18°C for 13 d after egg laying and shifted to 29°C for 48 h before dissection of the wing discs.

Adult wing imaging

Female adult flies were frozen upon collection with CO_2, with the wings removed for direct imaging. For the quantification, frozen female flies were dehydrated in serial solutions of EtOH (50%, 70% ×2, 90% ×2) for 10 min each, followed by 10 min in acetone. Flies were kept overnight in fresh acetone, and the wings were then mounted in Canada Balsam (Sigma; C1795-25ML). Wings, or representative adult females, were imaged with a Nikon SMZ1500 microscope

equipped with a Nikon DS-Fi1 camera controlled by NIS-Elements BR software.

Dissection and immunostaining

Wing discs. Third instar larvae were dissected after being kept for 6 d after egg laying at 25°C. Cuticles with attached imaginal discs were fixed for 15 min with 4% formaldehyde (Sigma; F8775) in PBS (phosphate buffer saline; Sigma-Aldrich; P4417) at room temperature, washed with PBS with 0.1% Triton X-100 (Thermo Fisher; A16046; hereafter PBST), and incubated with 1% bovine serum albumin (BSA; New England Biolabs; B9000S) in PBST for 1 h at room temperature. Cuticles were incubated with primary antibodies and 1% BSA in PBST overnight at 4°C, washed in PBST, incubated overnight at 4°C with secondary antibodies and 1% BSA in PBST (including DAPI when applicable), and washed in PBST again. All antibodies and their concentrations are listed in Table 1. Finally, discs were separated from the cuticles and mounted in Vectashield (Vector Labs; H-1000). For samples not requiring immunostaining, for example, imaging direct fluorescence of E-cad::GFP, discs were immediately mounted following fixation and one round of washing in PBST.

Embryos and retinas (Supplemental Figure S3). *Drosophila* embryos were aged up to the desired developmental stage with 3-h collections at 25°C, followed by 21 h at 18°C. Embryos were then dechorionated in 50% commercial bleach solution in water for 4 min. Following extensive washing with deionized water, embryos were fixed with 1:1 4% formaldehyde in PBS:heptane (Fisher Chemical; H-0110-17) for 20 min with constant agitation at room temperature. Embryos were devitellinized by vigorous shaking in 1:1 methanol:heptane for 20 s, washed, and stored in methanol at –20°C until required. Methanol was removed by washing in PBST, and embryos were subjected to the same staining procedure as the wing discs but using 0.05% Triton in PBS rather than 0.1%.

Prepupal stage individuals raised at 25°C were collected and aged for 40 h at 25°C to reach the desired developmental stage. Retinas were extracted by cutting the external cuticle open in PBS. The same protocol as for wing discs was followed for staining.

Pulse-chase assay

Wing discs were dissected in Schneider's Insect Medium (Life Technologies; 21720-024) with 1% Penstrep (Sigma-Aldrich; P0781-M100ML) and 5% fetal bovine serum (FBS; Life Technologies; 11543407), and the peripodial membrane was removed with a fine needle. Then, the discs were incubated with rat anti–E-cad antibody (DCAD2; 1:200; Developmental Studies Hybridoma Bank) in the same medium at 4°C for 1 h. After three quick washes with antibody-free cold medium, the discs were incubated in fresh antibody-free medium at room temperature for 10, 30, or 60 min. Several (five to seven) discs were fixed in 4% formaldehyde in PBS for 15 min at each analyzed time point (immediately after washing for $t = 0$ min). The discs were stained as described above using Alexa Fluor 488–conjugated anti-rat antibody (Jackson ImmunoResearch).

FRAP

Wing discs were dissected in Shield and Sang M3 Insect Medium (Sigma; S3652-500 ml) with 1% Penstrep (Sigma-Aldrich; P0781-M100ML) and 5% FBS (Life Technologies; 11543407) and placed into an observation chamber with a poly-D-lysine–coated coverslip (Aldaz *et al.*, 2010). Then, the medium was replaced by Shield and Sang M3 Insect Medium supplemented with methyl cellulose (Sigma; M0387-100G). Discs were positioned carefully to adhere to the coverslip and covered with an oxygen semipermeable membrane (YSY 5793).

Microscopy

All microscopy experiments except colocalization analyses were done using an upright Olympus FV1000 confocal microscope with either 60×/1.40 NA (fluorescence intensity, FRAP, and cell morphology) or 20×/0.75 NA (tissue morphology) objectives. In the former case, images were taken in the dorsal region of the wing disc pouch (Figure 1B): for each disc and compartment a z-stack of six slices spaced by 0.38 µm was acquired capturing the complete span of the apical AJs. This z-spacing was used for all the acquisitions with the 60× objective, while 1 µm spacing was used for z-stacks done with the 20× objective. All the images were at 16-bit depth in Olympus binary image format. For FRAP, several circular regions of 1 µm radius were photobleached at junctions so that there was only one bleach event per cell. Photobleaching was performed with eight scans at 4 µs/pixel at 80% 405 laser power, resulting in the reduction of E-cad–GFP signal by 60–80%. Z-stacks were acquired just before photobleaching, immediately after photobleaching, and then at 20-s intervals for 15 min in total.

Images used for colocalization assays were taken using an inverted Zeiss LSM 880 Airyscan confocal microscope. Z-stacks of 20 slices spaced by 0.20 µm (AP-1µ::VFP colocalization) or 10 slices spaced by 0.18 µm (E-cad GFP colocalization) were taken with a 63×/1.40 NA objective. Raw 16-bit images were processed using Zeiss software (automatic mode) to obtain ".czi" files.

Image processing

Compartment size (wing discs and adult wings). Z-stacks with E-cad::GFP and CD8::Cherry signals were projected using the "maximum intensity" algorithm in Fiji (https://fiji.sc) and used to measure the area of the whole disc and posterior compartment, respectively, with the Fiji selection tool. The anterior compartment area was calculated by subtracting the posterior compartment area from that of the disc. For adult wings, the posterior compartment was measured with the Fiji selection tool using vein L4 as its border, while vein L3 acted as the border of the anterior compartment, leaving out the area between the two veins.

Apical cell area and membrane and cytoplasmic protein levels. For the analyses of membrane and cytoplasmic protein levels, z-stacks with signal of GFP fluorescence were projected using the "average intensity" algorithm in Fiji. To distinguish membrane and cytoplasm as well as to measure apical cell area, we generated binary masks from images with visualized cell outlines (i.e., E-cad signal). In particular, z-stacks with E-cad signal were projected using the "maximum intensity" algorithm in Fiji. The background was subtracted from these projections using a rolling ball of 50-pixel radius, and their brightness and contrast were adjusted using the automatic optimization algorithm in Fiji. These projections were used to generate masks using the Tissue Analyzer plug-in in Fiji (Aigouy *et al.*, 2010). Cells in which the AJs were not completely in focus were removed manually.

The binary masks were used to measure the fluorescence intensity of average projections using our in-house MATLAB script (https://github.com/nbul/Intensity). First, individual objects (cells) and their boundaries were identified from each binary mask. Then the identified objects (cells) were analyzed on a cell-by-cell basis. The area of objects and length of their boundaries in pixels were determined and then manually converted from pixels to μm^2. The boundary was dilated using a diamond-shaped morphological

Reagent/resource	Source	ID/catalogue number
Drosophila strains		
; engrailed-GAL4;	Bloomington Drosophila Stock Center	BDSC #30564, Flybase: FBal0052377
MS1096-GAL4;;	Bloomington Drosophila Stock Center	BDSC #8860; Flybase: FBal0040476
; Act5C-GAL4;	Bloomington Drosophila Stock Center	BDSC #24414; Flybase: FBti0012293
w[1118];;	Bloomington Drosophila Stock Center	BDSC # 3605, Flybase: FBal0018186
;; UAS-Ap-1μ RNAi	Bloomington Drosophila Stock Center, Transgenic RNAi Project (HMS)	BDSC #27534, TRiP: JF02685
;; UAS-Ap-1γ RNAi	Bloomington Drosophila Stock Center, Transgenic RNAi Project (HMS)	BDSC #27533, TRiP: JF02684
;; UAS-CD8::Cherry	Bloomington Drosophila Stock Center	BDSC #27392, Flybase: FBtp0040985
;; UAS-p35	Bloomington Drosophila Stock Center	BDSC #5073, Flybase: FBst0005073
; tubulin::Gal80[ts];	Bloomington Drosophila Stock Center	BDSC #7019, FlyBase: FBti0027796
;; UAS-myr::GFP	Bloomington Drosophila Stock Center	BDSC # 58720, Flybase: FBti0164939
; shg-E-cadherin::GFP;	Bloomington Drosophila Stock Center	BDSC #60584, Flybase: FBti0168565
; Ubi-p63E-E::cadherin-GFP;	Kyoto Stock Center	Kyoto #109007, Flybase: FBal0122908
; shg^{IG27};	Gift from David Strutt, University of Sheffield, UK (Warrington *et al.*, 2013)	Flybase: FBal0327524
; UAS-diβ;	Gift from Nick Brown, University of Cambridge, UK (Domínguez-Giménez *et al.*, 2007)	N/A
; UAS-AP1μ::VFP;	Bloomington Drosophila Stock Center	BDSC #64260, Flybase: FBti0180780
;; UAS-P120ctn	Greig and Bulgakova, 2020a	Flybase: FBtp0143954
Antibodies		
Mouse anti-αPS1 integrin 1:10	Developmental Studies Hybridoma Bank	Cat#DK.1A4
Rat anti–E-cad 1:200	Developmental Studies Hybridoma Bank	Cat#DCAD2
Mouse anti-Wingless 1:50	Developmental Studies Hybridoma Bank	Cat#4D4
Mouse anti-Patched 1:10	Developmental Studies Hybridoma Bank	Cat#Apa1.3
Rabbit anti-Ph3 1:1000	Abcam	Cat#ab5176
Rabbit anti-cleaved Dcp-1 (asp216) 1:100	Cell Signaling Technology	Cat#9578s
Mouse anti–AP-1γ 1:100	Gift from R Le Borgne, University of Rennes, France (Benhra *et al.*, 2011)	N/A
Rabbit anti-Rab11 1:1000	Gift from Tsubasa Tanaka, RIKEN Center for Developmental Biology, Japan (Tanaka *et al.*, 2008)	N/A
Mouse anti-*Drosophila* Golgi mab 1:500	Calbiochem (Stanley *et al.*, 1997)	Currently unavailable
Goat anti-Golgin-245 (TGN) 1:2000	Developmental Studies Hybridoma Bank (Riedel *et al.*, 2016)	Cat#Golgin245
Mouse anti-βPS 1:100	Developmental Studies Hybridoma Bank	Cat#CF.6G11
Rabbit anti-Laminin B2 1:250	Abcam	Cat#ab47651
Mouse anti-phosphoJNK (Thr183/Tyr185) 1:300	Cell Signaling Technology	Cat#9255

TABLE 1: Reagents and tools.

(Continues)

Reagent/resource	Source	ID/catalogue number
Donkey anti-rat Alexa Fluor 488 (1:300)	Jackson ImmunoResearch	Cat#712-545-153
Donkey anti-rat Alexa Fluor 647 (1:300)	Jackson ImmunoResearch	Cat#712-605-153
Donkey anti-mouse Alexa Fluor 488 (1:300)	Jackson ImmunoResearch	Cat#715-545-151
Donkey anti-mouse Alexa Fluor 647 (1:300)	Jackson ImmunoResearch	Cat#715-605-151
Donkey anti-goat Alexa Fluor 647 (1:300)	Jackson ImmunoResearch	Cat#705-605-147
Donkey anti-rabbit Alexa Fluor 647 (1:300)	Jackson ImmunoResearch	Cat#711-605-152
Oligonucleotides and other sequence-based reagents		
Ap-1μ Fw 5′-CGCTTCGAGAATGACCGGAC-3′	This study	N/A
Ap-1μ Rv 5′-ATGCCGCTCGATCACTGATTC-3′		
Ap-1γ Fw 5′-ACCTGCTTATCACCAACTGCT-3′		
Ap-1γ Rv 5′-CAGAGTGCATAGGGCTAGGC-3′		
shg Fw 5′-TCCATGGTCGGAAAATGCCCA-3′		
shg Rv 5′-AGTACTGAAAGTCGCGCTCC-3′		
Actin5C Fw 5′-GGACCGGACTCGTCATACTC-3-3′	Barber *et al.*, 2016	
Actin5C Rv 5′-CTGGCGGCACTACCATGTATC-3′		
Chemicals, enzymes, and other reagents		
PBS	Sigma-Aldrich	Cat#P4417-50TAB
Formaldehyde solution (40%)	Sigma-Aldrich	Cat#F8775
Triton X-100	Thermo Fisher	Cat#A16046
BSA	New England Biolabs	Cat#B9000S
DAPI 1:200	Thermo Fisher	Cat#D1306
Vectashield mounting media	Vector Labs	Cat#H-1000
Bleach	Arco Essentials	Cat#5540012
Heptane	Fisher Chemical	Cat#H/0110/17
Schenider's *Drosophila* medium	Life Technologies (Thermo Fisher)	Cat#21720-024
Shield and Sang M3 Insect Medium	Sigma-Aldrich	Cat#S3652-500ML
FBS	Life Technologies (Thermo Fisher)	Cat#11543407
Penicillin–streptomycin (Penstrep)	Sigma-Aldrich	Cat#P0781-M100ML
Methyl cellulose	Sigma-Aldrich	Cat#M0387-100G
Canada Balsam	Sigma-Aldrich	Cat#C1795-25ML
Semi-permeable membranes	YSI	Cat#5793
Acetone	Fisher Scientific	Cat#A18-500

TABLE 1: Reagents and tools.

(Continues)

Reagent/resource	Source	ID/catalogue number
Software		
NIS-Elements BR	Nikon	N/A
FV10-ASW	Olympus	N/A
Zen	Zeiss	N/A
Fiji (ImageJ)	https://fiji.sc	N/A
Tissue analyzer	Benoit Aigouy (Aigouy *et al.*, 2010)	N/A
MATLAB R2019b	Mathworks	N/A
GraphPad Prism Version 7	GraphPad Software	N/A
Office Excel 16	Microsoft	N/A
Illustrator 20	Adobe	N/A
Custom scripts for MATLAB	Natalia Bulgakova (https://github.com/nbul)	N/A
Other		
NucleoSpin RNA XS Kit	Macherey-Nagel	Cat#740902.50
High-Capacity RNA-to-cDNA Kit	Applied Biosystems	Cat#4387406
SYBR Green JumpStart Taq Ready MixTM	Sigma-Aldrich	Cat#S4438
SMZ1500 microscope with DS-Fi1 camera	Nikon	N/A
FV1000 confocal microscope	Olympus	N/A
LSM 880 Airyscan Microscope	Zeiss	N/A
NanoDrop ND-1000	Thermo Fisher	N/A
PTC-200 Peltier Thermal Cycler	MJ Research	N/A
CFX96 C1000 Touch Thermal Cycler	Bio-Rad	N/A

TABLE 1: Reagents and tools. Continued

structural element of size 3 to encompass the *XY* spread of E-cad signal. The mean and total (sum of all pixel intensities) intensities of the dilated boundary (membrane signal) and the object with subtracted boundary (cytoplasm) were calculated. All the values were averaged to produce single values per wing disc, thus testing biological replicates and excluding chances of one disc having a higher contribution to the result due to the variable number of cells in each disc.

Proliferation. Z-stacks with E-cad::GFP and pH3 (647) signal corresponding to the anterior and posterior dorsal wing pouches were processed separately for each channel. E-cad signal was segmented as described above using Tissue Analyzer. The resulting binary masks were dilated and then inverted. The area with cells was used then to generate maximum projections of the equivalent region for the pH3 channel. The projection was processed using the following steps: background was subtracted using a rolling ball of 1-pixel radius; then Gaussian blur of 2-pixel radius was added; and image was binarized using a threshold set to three times the average intensity of the original maximum projection.

To calculate the cell number and the total cell area in the imaged regions from the processed binary segmented masks, we employed the Fiji Particle Analysis plug-in, limiting particle detection to sizes up to 67.5 μm^2 (or 3000 $pixel^2$). The number of proliferating cells in the same area was determined using the processed images of the pH3 channel corresponding to the same area using particle sizes between 5 and 50 μm^2. These numbers were used to calculate the number of dividing cells per 100 cells or per 100 μm^2.

Colocalization. For colocalization of AP-1μ::VFP with cellular markers as well as E-cad::GFP with AP-1γ antibody, we employed the colocalization plug-in Coloc 2 in Fiji (https://imagej.net/Coloc2) and performed the analysis section by section. We selected Manders's colocalization coefficients (MCC [Manders *et al.*, 1993; McDonald and Dunn, 2013]) as more informative for probes distributed to more than one compartment than Pearson's correlation coefficients (Dunn *et al.*, 2011). The MCC_{diff} value was obtained by subtracting the percentage of pixels positive for AP-1μ::VFP (obtained using the threshold determined by Coloc 2) from the percentage of pixels positive for the marker that were also positive for AP-1μ::VFP.

For colocalization of E-cad::GFP with Golgi bodies and recycling endosomes, we analyzed the images again section by section, but with an in-house script at MATLAB (https://github.com/nbul/Localization). This script followed the same principle to obtain MCC_{diff} values as the Coloc 2 plug-in but is more versatile as it enables a manual selection of a threshold method for each probe. Such selection is required as the bright signal of E-cad::GFP at cell borders limits its detection in cytoplasm using standard threshold methods. The E-cad::GFP signal at cell borders was excluded from the analysis, and the resulting MCC_{diff} values accounted therefore only for the intracellular signal.

Pulse-chase. Twelve sections, comprising six sections spanning the complete region of AJs visualized with the staining of the antibody bound to E-cad at the cell surface and the six sections immediately basal to AJs, were used for counting the E-cad–positive vesicles. First, a binary mask with cell outlines was created from a projection of the six apical-most sections as described above. The average cytoplasmic signal and cell area were measured with our in-house script as described above and used to threshold the corresponding maximum projection of the six basal sections in Fiji using the following steps: background was subtracted using a rolling ball of 4-pixel radius; then Gaussian blur of 2-pixel radius was added; and the image was binarized using a threshold set to 70% of the average cytoplasmic signal of the apical section. The resulting images were used for the analysis using the Particle Analysis plug-in in Fiji, limiting particle detection to sizes between 0.01 and 0.45 μm^2. The parameters were empirically selected through interactive validation. Puncta density was determined using the average apical area of the cells.

FRAP. Z-stacks for each time point in the time series were projected using the "average intensity" algorithm in Fiji. The recovery curves were obtained by manually measuring intensities of background, control region, and photobleached region using 2-μm-diameter circular regions for each time point in Fiji. The raw data were processed as in Greig and Bulgakova (2021) to obtain the normalized recovery curves, namely following background subtraction the intensity at the bleached spot was normalized to the intensities of a control area at the same time point and the bleached area before bleaching.

Cell death. Z-stacks of six slices corresponding to the basal region of the discs were projected using the "average intensity" in Fiji. E-cad antibody signal was used to generate a mask encompassing the whole disc pouch (all the disc ventral to the H/H fold, corresponding approximately to the domain of *MS1096* expression). Dcp-1 signal was processed twice with the "smoothening" tool and then thresholded with the Otsu method (automatic levels). Dcp-1 signal was measured as a percentage within the mask.

JNK signaling. JNK signaling. Z-stacks of 20 slices spanning the entire depth of discs were projected using the "average intensity" in Fiji. The binary masks were created in Fiji using the CD8::Cherry signal projections, and wing pouch regions were manually cropped. The mean pJNK intensity was measured in each projection using the created masks following an automatic background subtraction with a rolling ball with 50-pixel radius.

Other processing. Sagittal views of the wing discs, for example in Figure 1, were generated using the "Reslice" tool in Fiji. For representative cases shown in figures, maximum projections of the regions of interest were generated in Fiji using minimum modification, such as tilting, cropping, or automatic contrast of the whole view, for better presentation.

RT-qPCR

Primers for quantitative reverse transcription PCR (RT-qPCR) were designed and in silico tested using Flybase (https://flybase.org), Primer-BLAST (https://www.ncbi.nlm.nih.gov/tools/primer-blast/index.cgi), and Net Primer (http://www.premierbiosoft.com/netprimer/) tools and whenever possible aimed to target sequences separated by introns and present in all the splicing variants. All primers and amplicon sizes are listed in Table 1 and were manufactured by Thermo Fisher. RNA was extracted from wing discs dissected on ice using the NucleoSpin RNA XS Kit (Macherey-Nagel; 740902.50). Control wing discs expressed *UAS*-Myr::GFP instead of the RNAi. For AP-1γ knockdown, only discs from male larvae were used to exclude the potential effects of dosage compensation. RNA concentration was determined with an ND-1000 Spectrophotometer (Nanodrop; Thermo Fisher) and immediately used to generate cDNA with the High-Capacity RNA-to-cDNA Kit (Applied Biosystems; 4387406) using 400 ng of RNA. cDNA was then used as a template for the quantitative PCR using SYBR

Green JumpStart Taq Ready Mix (Sigma-Aldrich; S4438) using a CFX96 Real-Time System (Bio-Rad) and its proprietary software. All the primers were tested with standard reaction curves and gel electrophoresis. Upon testing of several widely employed housekeeping genes in *Drosophila* (Ponton *et al.*, 2011; Lü *et al.*, 2018), primers against *Actin5C* were selected due to their reproducible performance. Reactions were carried out in three technical replicates per biological replicate (15 wing discs), in a volume of 10 µl with a primer concentration of 1 pmol/µl. At least three biological replicates were done per genotype. Ct values were obtained from SYBR fluorescence using thresholds determined from the standard curves (Larionov *et al.*, 2005). Primer purity was tested on a control without any template in every performed assay.

Expression levels were determined by the $2^{-\Delta\Delta CT}$ method (Schmittgen and Livak, 2008). For each biological replicate, Ct values were averaged across all technical replicates; and the average Ct value of *Actin5C* was subtracted from the target gene. This result (ΔCT) was normalized by subtracting the average ΔCT of the control genotype, producing ΔΔCT. This value was converted using the formula $2^{-\Delta\Delta CT}$.

Statistical analysis

All the statistical analyses were done in GraphPad Prism 7 (https://graphpad.com/scientific-software/prism/). First, the data sets were confirmed to be free of detectable outliers using the ROUT detection method (Q = 0.1%), and the distributions were tested for being normal with the D'Agostino and Pearson test. Precise *n* numbers, the type of statistical test, and the type of represented data (i.e., individual cases, mean and SD, etc.) are described in the figure captions. Significance was visually depicted in all the graphs with either the precise value or symbols (*$p < 0.05$, **$p < 0.001$, ***$p < 0.0001$, ****$p < 0.00001$, $^{\#\#\#}p < 0.001$, and $^{\#\#\#\#}p < 0.0001$). For commonly used tests, such as the *t* test, two-tailed versions were used. Nonparametric tests were used when at least one sample did not display normal distribution, and appropriate corrections were applied if the assumption of equality of SDs was not met.

Posterior:anterior compartment size ratio. Posterior:anterior compartment size ratios of discs expressing RNAi against subunits of the AP-1 complex were tested against the external control discs expressing CD8::Cherry only using the Brown-Forsythe and Welch analysis of variance (ANOVA) test.

Proliferating cells. The number of dividing cells per 100 cells or per 100 µm^2 were compared with paired *t* test/Wilcoxon test (between compartments of the same genotype), and Kruskal–Wallis test (between genotypes and the anterior control compartment).

Protein levels and cell size. Differences between compartment pairs on different genotypes were tested with two-way ANOVA (Tukey's or Šidák's multiple comparison test). Single compartment comparison was performed with paired *t* test (normal distribution) or Wilcoxon test.

Colocalization. The differences between control and experimental compartments were tested using paired *t* test (normal distribution) or Wilcoxon test. The MCC_{diff} value was also tested against zero (random colocalization [McDonald and Dunn, 2013]) using the one-sample *t* test.

Pulse-chase. The puncta densities were compared between the compartments using Welch's *t* test.

FRAP. Each replicate value in each data set was considered as an individual point for curve fitting. GraphPad Prism software was used for nonlinear fitting using a biexponential model, $f(t) = 1 - F_{im} - A_1 \times e^{-t/Tfast} - A_2 \times e^{-t/Tslow}$, and a single exponential model, $f(t) = 1 - F_{im} - A_1 \times e^{-t/Tslow}$, where F_{im} is a size of the immobile pool of the protein, T_{fast} and T_{slow} are the halftimes, and A_1 and A_2 are the amplitudes of the fast and slow components of the recovery. An *F* test was used to choose the equation and compare data sets.

Expression analyses. The gene expression in RNAi-expressing samples was compared with myr::GFP-expressing controls using Welch's *t* test.

Dcp-1 area. The Dcp-1–positive wing pouch surface was compared between genotypes using an unpaired *t* test.

pJNK intensity. pJNK intensity in posterior compartments of wing pouches was compared between genotypes using an unpaired *t* test.

Data availability

The generated *Drosophila* strains are available upon request. All in-house scripts are available at https://github.com/nbul/.

ACKNOWLEDGMENTS

We thank Nick Brown, Iwan Evans, Roland Le Borgne, and Tsubasa Tanaka for reagents; the University of Sheffield's Wolfson Light Microscopy and Fly Facilities for their technical support; and Kyra Campbell and David Strutt for reagents and critical feedback on the manuscript. This work was supported by a grant from the Biotechnology and Biological Sciences Research Council, UK Research and Innovation (BB/P007503/1) to N.A.B. and a summer studentship from the Genetics Society and Think Ahead SURE scheme (University of Sheffield) to M.R.M. and K.B.

REFERENCES

Aigouy B, Farhadifar R, Staple DB, Sagner A, Roper JC, Julicher F, Eaton S (2010). Cell flow reorients the axis of planar polarity in the wing epithelium of Drosophila. Cell 142, 773–786.

Aldaz S, Escudero LM, Freeman M (2010). Live imaging of Drosophila imaginal disc development. Proc Natl Acad Sci USA 107, 14217–14222.

Barber AF, Erion R, Holmes TC, Sehgal A (2016). Circadian and feeding cues integrate to drive rhythms of physiology in Drosophila insulin-producing cells. Genes Dev 30, 2596–2606.

Bellec K, Pinot M, Gicquel I, Le Borgne R (2021). The clathrin adaptor AP-1 and Stratum act in parallel pathways to control Notch activation in Drosophila sensory organ precursors cells. Development 148, dev191437.

Benhra N, Lallet S, Cotton M, Le Bras S, Dussert A, Le Borgne R (2011). AP-1 controls the trafficking of Notch and Sanpodo toward E-cadherin junctions in sensory organ precursors. Curr Biol 21, 87–95.

Bergantiños C, Corominas M, Serras F (2010). Cell death-induced regeneration in wing imaginal discs requires JNK signalling. Development 137, 1169–1179.

Bonifacino JS (2014). Adaptor proteins involved in polarized sorting. J Cell Biol 204, 7–17.

Bonifacino JS, Rojas R (2006). Retrograde transport from endosomes to the trans-Golgi network. Nat Rev Mol Cell Biol 7, 568–579.

Brand AH, Perrimon N (1993). Targeted gene expression as a means of altering cell fates and generating dominant phenotypes. Development (Cambridge, England) 118, 401–415.

Brower DL, Wilcoxt M, Piovant M, Smiths RJ, Reger LA (1984). Related cell-surface antigens expressed with positional specificity in Drosophila imaginal discs. Proc Natl Acad Sci USA 81, 7485–7489.

Brüser L, Bogdan S (2017). Adherens junctions on the move—membrane trafficking of E-cadherin. Cold Spring Harb Perspect Biol 9, a029140.

Bulgakova NA, Brown NH (2016). Drosophila p120-catenin is crucial for endocytosis of the dynamic E-cadherin-Bazooka complex. J Cell Sci 129, 477–482.

Bulgakova NA, Grigoriev I, Yap AS, Akhmanova A, Brown NH (2013). Dynamic microtubules produce an asymmetric E-cadherin-Bazooka complex to maintain segment boundaries. J Cell Biol 201, 887–901.
Burgess J, Jauregui M, Tan J, Rollins J, Lallet S, Leventis PA, Boulianne GL, Chang HC, Le Borgne R, Krämer H, Brill JA (2011). AP-1 and clathrin are essential for secretory granule biogenesis in Drosophila. Mol Biol Cell 22, 2094–2105.
Coffman VC, Wu J-Q (2012). Counting protein molecules using quantitative fluorescence microscopy. Trends Biochem Sci 37, 499–506.
Domínguez-Giménez P, Brown NH, Martín-Bermudo MD (2007). Integrin-ECM interactions regulate the changes in cell shape driving the morphogenesis of the Drosophila wing epithelium. J Cell Sci 120, 1061–1071.
D'Souza-Schorey C, Li G, Colombo MI, Stahl PD (1995). A regulatory role for ARF6 in receptor-mediated endocytosis. Science 267, 1175–1178.
Dunn KW, Kamocka MM, McDonald JH (2011). A practical guide to evaluating colocalization in biological microscopy. Am J Physiol Cell Physiol 300, C723–C742.
Eaton S, Martin-Belmonte F (2014). Cargo sorting in the endocytic pathway: a key regulator of cell polarity and tissue dynamics. Cold Spring Harb Perspect Biol 6, a016899.
Fan Y, Bergmann A (2008). Apoptosis-induced compensatory proliferation. The cell is dead. Long live the cell! Trends Cell Biol 18, 467–473.
Fölsch H (2015). Role of the epithelial cell-specific clathrin adaptor complex AP-1B in cell polarity. Cell Logist 5, e1074331.
Fölsch H, Pypaert M, Maday S, Pelletier L, Mellman I (2003). The AP-1A and AP-1B clathrin adaptor complexes define biochemically and functionally distinct membrane domains. J Cell Biol 163, 351–362.
Fölsch H, Pypaert M, Schu P, Mellman I (2001). Distribution and function of Ap-1 clathrin adaptor complexes in polarized epithelial cells. J Cell Biol 152, 595–606.
Gillard G, Shafaq-Zadah M, Nicolle O, Damaj R, Pecreaux J, Michaux G (2015). Control of E-cadherin apical localisation and morphogenesis by a SOAP-1/AP-1/clathrin pathway in C. elegans epidermal cells. J Cell Sci 128, e1007.
Grant BD, Donaldson JG (2009). Pathways and mechanisms of endocytic recycling. Nat Rev Mol Cell Biol 10, 597–608.
Gravotta D, Carvajal-Gonzalez JM, Mattera R, Deborde S, Banfelder JR, Bonifacino JS, Rodriguez-Boulan E (2012). The clathrin adaptor AP-1A mediates basolateral polarity. Dev Cell 22, 811–823.
Gravotta D, Deora A, Perret E, Oyanadel C, Soza A, Schreiner R, Gonzalez A, Rodriguez-Boulan E (2007). AP1B sorts basolateral proteins in recycling and biosynthetic routes of MDCK cells. Proc Natl Acad Sci USA 104, 1564–1569.
Greig J, Bulgakova NA (2020a). Arf6 determines tissue architecture by stabilizing intercellular adhesion. Philos Trans R Soc Lond B Biol Sci 375, 20190682.
Greig J, Bulgakova NA (2020b). Interplay between actomyosin and E-cadherin dynamics regulates cell shape in the Drosophila embryonic epidermis. J Cell Sci 133, jcs242321.
Greig J, Bulgakova NA (2021). Fluorescence recovery after photobleaching to study the dynamics of membrane-bound proteins in vivo using the Drosophila embryo. Methods Mol Biol 2179, 145–159.
Gumbiner BM (1996). Cell adhesion: the molecular basis of tissue architecture and morphogenesis. Cell 84, 345–357.
Guo Y, Chang C, Huang R, Liu B, Bao L, Liu W (2012). AP1 is essential for generation of autophagosomes from the trans-Golgi network. J Cell Sci 125, 1706–1715.
Halbleib JM, Nelson WJ (2006). Cadherins in development: cell adhesion, sorting, and tissue morphogenesis. Genes Dev 20, 3199–3214.
Hariharan IK, Bilder D (2006). Regulation of imaginal disc growth by tumor-suppressor genes in Drosophila. Annu Rev Genet 40, 335–361.
Harris TJC, Peifer M (2004). Adherens junction-dependent and -independent steps in the establishment of epithelial cell polarity in Drosophila. J Cell Biol 167, 135–147.
Hase K, Nakatsu F, Ohmae M, Sugihara K, Shioda N, Takahashi D, Obata Y, Furusawa Y, Fujimura Y, Yamashita T, *et al.* (2013). AP-1B–mediated protein sorting regulates polarity and proliferation of intestinal epithelial cells in mice. Gastroenterology 145, 625–635.
Hay BA, Wolff T, Rubin GM (1994). Expression of baculovirus P35 prevents cell death in Drosophila. Development 120, 2121–2129.
Heisenberg C-P, Bellaïche Y (2013). Forces in tissue morphogenesis and patterning. Cell 153, 948–962.
Herrera SC, Martín R, Morata G (2013). Tissue homeostasis in the wing disc of Drosophila melanogaster: immediate response to massive damage during development. PLoS Genet 9, e1003446.
Herrmann JM, Spang A (2015). Intracellular Parcel Service: Current Issues in Intracellular Membrane Trafficking, New York: Humana Press, 1–12.
Huang J, Zhou W, Dong W, Watson AM, Hong Y (2009). From the cover: directed, efficient, and versatile modifications of the Drosophila genome by genomic engineering. Proc Natl Acad Sci USA 106, 8284–8289.
Huang Y, Ma T, Lau PK, Wang J, Zhao T, Du S, Loy MMT, Guo Y (2019). Visualization of protein sorting at the trans-Golgi network and endosomes through super-resolution imaging. Front Cell Dev Biol 7, 181.
Iyer KV, Piscitello-Gómez R, Paijmans J, Jülicher F, Eaton S (2019). Epithelial viscoelasticity is regulated by mechanosensitive E-cadherin turnover. Curr Biol 29, 578-591.e5.
Janiszewska M, Primi MC, Izard T (2020). Cell adhesion in cancer: beyond the migration of single cells. J Biol Chem 295, 2495–2505.
Jezowska B, Fernández BG, Amândio AR, Duarte P, Mendes C, Brás-Pereira C, Janody F (2011). A dual function of Drosophila capping protein on DE-cadherin maintains epithelial integrity and prevents JNK-mediated apoptosis. Dev Biol 360, 143–159.
Kametaka S, Kametaka A, Yonekura S, Haruta M, Takenoshita S, Goto S, Waguri S (2012). AP-1 clathrin adaptor and CG8538/Aftiphilin are involved in Notch signaling during eye development in Drosophila melanogaster. J Cell Sci 125, 634–648.
Kell MJ, Ang SF, Pigati L, Halpern A, Fölsch H (2020). Novel function for AP-1B during cell migration. Mol Biol Cell 31, 2475–2493.
Kondylis V, Rabouille C (2009). The Golgi apparatus: lessons from Drosophila. FEBS Lett 583, 3827–3838.
Kumari S, Mayor S (2008). ARF1 is directly involved in dynamin-independent endocytosis. Nat Cell Biol 10, 30–41.
Larionov A, Krause A, Miller W (2005). A standard curve based method for relative real time PCR data processing. BMC Bioinform 6, 62.
Lee JL, Streuli CH (2014). Integrins and epithelial cell polarity. J Cell Sci 127, 3217–3225.
Lefkir Y, Malbouyres M, Gotthardt D, Ozinsky A, Cornillon S, Bruckert F, Aderem AA, Soldati T, Cosson P, Letourneur F (2004). Involvement of the AP-1 adaptor complex in early steps of phagocytosis and macropinocytosis. Mol Biol Cell 15, 861–869.
Ling K, Bairstow SF, Carbonara C, Turbin DA, Huntsman DG, Anderson RA (2007). Type Iγ phosphatidylinositol phosphate kinase modulates adherens junction and E-cadherin trafficking via a direct interaction with μ1B adaptin. J Cell Biol 176, 343–353.
Loyer N, Kolotuev I, Pinot M, Le Borgne R (2015). Drosophila E-cadherin is required for the maintenance of ring canals anchoring to mechanically withstand tissue growth. Proc Natl Acad Sci USA 112, 12717–12722.
Lü J, Yang C, Zhang Y, Pan H (2018). Selection of reference genes for the normalization of RT-qPCR data in gene expression studies in insects: a systematic review. Front Physiol 9, 1560.
Manders EMM, Verbeek FJ, Aten JA (1993). Measurement of co-localization of objects in dual-colour confocal images. J Microsc 169, 375–382.
Martín FA, Peréz-Garijo A, Morata G (2009). Apoptosis in Drosophila: compensatory proliferation and undead cells. Int J Dev Biol 53, 1341–1347.
Martin-Bermudo MD, Brown NH, Jan LY, Jan YN (1999). Uncoupling integrin adhesion and signaling: the beta PS cytoplasmic domain is sufficient to regulate gene expression in the Drosophila embryo. Genes Dev 13, 729–739.
McDonald JH, Dunn KW (2013). Statistical tests for measures of colocalization in biological microscopy. J Microsc 252, 295–302.
Nakatsu F, Hase K, Ohno H, Nakatsu F, Hase K, Ohno H (2014). The role of the clathrin adaptor AP-1: polarized sorting and beyond. Membranes 4, 747–763.
Nanes BA, Kowalczyk AP (2012). Adherens junction turnover: regulating adhesion through cadherin endocytosis, degradation, and recycling. Subcell Biochem 60, 197–222.
Oda H, Tsukita S (2001). Real-time imaging of cell-cell adherens junctions reveals that Drosophila mesoderm invagination begins with two phases of apical constriction of cells. J Cell Sci 114, 493–501.
Palamidessi A, Frittoli E, Ducano N, Offenhauser N, Sigismund S, Kajiho H, Parazzoli D, Oldani A, Gobbi M, Serini G, *et al.* (2013). The GTPase-activating protein RN-tre controls focal adhesion turnover and cell migration. Curr Biol 23, 2355–2364.
Pérez-Garijo A, Shlevkov E, Morata G (2009). The role of Dpp and Wg in compensatory proliferation and in the formation of hyperplastic overgrowths caused by apoptotic cells in the Drosophila wing disc. Development 136, 1169–1177.
Ponton F, Chapuis M-P, Pernice M, Sword GA, Simpson SJ (2011). Evaluation of potential reference genes for reverse transcription-qPCR studies of physiological responses in Drosophila melanogaster. J Insect Physiol 57, 840–850.

Ramirez Moreno M, Stempor P, Bulgakova N (2021). Interactions and feedbacks in E-cadherin transcriptional regulation. Front Cell Dev Biol 9, 701175.
Ren X, Farías GG, Canagarajah BJ, Bonifacino JS, Hurley JH (2013). Structural basis for recruitment and activation of the AP-1 clathrin adaptor complex by Arf1. Cell 152, 755–767.
Riedel F, Gillingham AK, Rosa-Ferreira C, Galindo A, Munro S (2016). An antibody toolkit for the study of membrane traffic in Drosophila melanogaster. Biol Open 5, 987–992.
Robinson MS (2004). Adaptable adaptors for coated vesicles. Trends Cell Biol 14, 167–174.
Sauvageau E, McCormick PJ, Lefrancois S (2017). In vivo monitoring of the recruitment and activation of AP-1 by Arf1. Sci Rep 7, 7148.
Schmittgen TD, Livak KJ (2008). Analyzing real-time PCR data by the comparative CT method. Nat Protoc 3, 1101–1108.
Schock F, Perrimon N (2002). Molecular mechanisms of epithelial morphogenesis. Annu Rev Cell Dev Biol 18, 463–493.
Shafaq-Zadah M, Brocard L, Solari F, Michaux G (2012). AP-1 is required for the maintenance of apico-basal polarity in the C. elegans intestine. Development (Cambridge, England) 139, 2061–2070.
Shteyn E, Pigati L, Fölsch H (2011). Arf6 regulates AP-1B-dependent sorting in polarized epithelial cells. J Cell Biol 194, 873–887.
Sprague BL, McNally JG (2005). FRAP analysis of binding: proper and fitting. Trends Cell Biol 15, 84–91.
Stamnes MA, Rothman JE (1993). The binding of AP-1 clathrin adaptor particles to Golgi membranes requires ADP-ribosylation factor, a small GTP-binding protein. Cell 73, 999–1005.
Stanley H, Botas J, Malhotra V (1997). The mechanism of Golgi segregation during mitosis is cell type-specific. Proc Natl Acad Sci USA 94, 14467–14470.
Sui L, Alt S, Weigert M, Dye N, Eaton S, Jug F, Myers EW, Jülicher F, Salbreux G, Dahmann C (2018). Differential lateral and basal tension drive folding of Drosophila wing discs through two distinct mechanisms. Nat Commun 9, 4620.
Takeichi M (1977). Functional correlation between cell adhesive properties and some cell surface proteins. J Cell Biol 75, 464–474.
Tan JZA, Gleeson PA, Tan JZA, Gleeson PA (2019). Cargo sorting at the trans-Golgi network for shunting into specific transport routes: role of Arf small G proteins and adaptor complexes. Cells 8, 531.
Tanaka T, Nakamura A, Michaud J, Cohen RS (2008). The endocytic pathway acts downstream of Oskar in Drosophila germ plasm assembly. Development (Cambridge, England) 135, 1107–1117.
Warrington SJ, Strutt H, Strutt D (2013). The Frizzled-dependent planar polarity pathway locally promotes E-cadherin turnover via recruitment of RhoGEF2. Development 140, 1045–1054.
Weiss RA (2004). Multistage carcinogenesis. Br J Cancer 91, 1981–1982.
Wrobel AG, Kadlecova Z, Kamenicky J, Yang JC, Herrmann T, Kelly BT, McCoy AJ, Evans PR, Martin S, Müller S, *et al*. (2019). Temporal ordering in endocytic clathrin-coated vesicle formation via AP2 phosphorylation. Dev Cell 50, 494–508.e11.
Wu J-Q, Pollard TD (2005). Counting cytokinesis proteins globally and locally in fission yeast. Science 310, 310–314.
Xiao K, Oas RG, Chiasson CM, Kowalczyk AP (2007). Role of p120-catenin in cadherin trafficking. Biochim Biophys Acta 1773, 8–16.
Yamada KM, Miyamoto S (1995). Integrin transmembrane signaling and cytoskeletal control. Curr Opin Cell Biol 7, 681–689.
York HM, Coyle J, Arumugam S (2020). To be more precise: the role of intracellular trafficking in development and pattern formation. Biochem Soc Trans 48, 2051–2066.